

THESIS

IMAGE-BASED DEVELOPMENT OF THREE-DIMENSIONAL  
FINITE ELEMENT MODELS

Submitted by

Xin Huang

Department of Civil and Environmental Engineering

In partial fulfilment of the requirements

For the Degree of Master of Science

Colorado State University

Fort Collins, Colorado

Summer 2018

Master's Committee:

Advisor: Paul R. Heyliger

Rebecca A. Atadero

Kirk McGilvray

Copyright by Xin Huang 2018  
All Rights Reserved

## ABSTRACT

### IMAGE-BASED DEVELOPMENT OF THREE-DIMENSIONAL FINITE ELEMENT MODELS

In the finite element method (FEM), constructing three-dimensional (3D) models of irregular geometries of structures can be technically difficult and cost-inefficient due to the requirement for expensive equipment such as three-dimensional laser scanner. Along with the rapid development of photogrammetry in 3D modeling, an appropriate application of advanced photogrammetric technologies in FEM can greatly facilitate productivity where analysis of a large number of irregular geometries is needed. In this study, a quasi-automatic, user-friendly approach to construct 3D finite element models using advanced techniques in the field of photogrammetry is introduced and successfully applied to example geometries of structural mechanics. The 3D models were constructed in a photogrammetric program from 2D photo sequences taken by ordinary commercial cameras and then analyzed in a FEM software package. General guidance of using photogrammetric approach to acquire feasible 3D models for FEM analysis was also included. Convergence of stresses and deformation of the structure were found in the analyses with increasing number of discretized elements. The approach introduced in this thesis is recommended for the FEM analyses of structures with irregular geometries and homogeneous materials when conventional methods are less effective due to the difficult modeling process.

## ACKNOWLEDGMENT

I acknowledge Dr. Heyliger for providing insights and methodological assistance in this study and helping to improve the coherence of the thesis.

I thank Chao Jiang for providing me the guidance of using Agisoft PhotoScan and her great assistance of 3D modeling.

I would also like to show my gratitude to Chuanjin Zhang for providing the unmanned drone photos of Newton's Corner.

## TABLE OF CONTENTS

ABSTRACT . . . . .	ii
ACKNOWLEDGMENT . . . . .	iii
LIST OF FIGURES . . . . .	vi
LIST OF TABLES . . . . .	viii
1 INTRODUCTION AND LITERATURE REVIEW . . . . .	1
1.1 Overview . . . . .	1
1.2 Literature Review . . . . .	3
1.2.1 Surveying . . . . .	3
1.2.2 Topographic Mapping . . . . .	3
1.2.3 Structural Engineering . . . . .	4
2 METHODS . . . . .	6
2.1 Introduction . . . . .	6
2.2 Preparation of Photo Sequence . . . . .	8
2.2.1 Details of Surface . . . . .	8
2.2.2 Reflective Surfaces . . . . .	9
2.2.3 Lighting Condition . . . . .	9
2.2.4 Overlap . . . . .	10
2.2.5 Targets . . . . .	10
2.3 Use of Photogrammetric Software . . . . .	11
2.3.1 Photo Alignment . . . . .	11
2.3.2 Model Construction . . . . .	13
2.3.3 Masking . . . . .	14
2.3.4 Manifold Solid Model . . . . .	15
2.4 Imaging of Systems . . . . .	16
2.4.1 Highway Guardrail . . . . .	16
2.4.2 Newton's Corner . . . . .	18
2.4.3 Coffee Mug . . . . .	19

2.4.4	Tissue Roll . . . . .	21
2.4.5	Clock Tower . . . . .	22
2.4.6	Metate Arch . . . . .	24
2.4.7	Dilitant Fault . . . . .	27
2.5	Repair for Non-Manifold Model . . . . .	28
2.6	Discretization . . . . .	30
2.6.1	Model Size . . . . .	30
2.6.2	Removing Virtual Topography . . . . .	31
2.6.3	Mesh Size . . . . .	32
3	RESULTS . . . . .	33
4	SUMMARY & CONCLUSION . . . . .	40
	REFERENCES . . . . .	42
	APPENDIX A: Output Data of Analysis for Dilitant Fault . . . . .	45

## LIST OF FIGURES

1	Metate Arch and Dilitant Fault . . . . .	2
2	Flowchart of Method Used in this Thesis . . . . .	7
3	3D Models of Imaged Systems . . . . .	7
4	2D Drawing of A 3D Object Without Sufficient Details . . . . .	9
5	Printable Targets Provided by Agisoft PhotoScan . . . . .	10
6	Positions of Camaras of Aligned Photos in Agisoft PhotoScan . . . . .	11
7	Contrast of 3D Surface Model with Modification of Sparse Point Cloud . . . . .	12
8	Contrast of 3D Surface Model with Interpolation . . . . .	14
9	Example of 3D Surface Models with Different Numbers of Faces . . . . .	14
10	Contrast of 3D Surface Models Constructed with Masks of Photos . . . . .	15
11	Example of Using Close Hole Tool in Agisoft PhotoScan . . . . .	16
12	Guardrail at Exit 268 of I25, Colorado . . . . .	17
13	3D Model of Newton’s Corner . . . . .	19
14	Models of A Coffee Mug Constructed Using Masks . . . . .	20
15	Example of A Poor-Quality 3D Surface Model . . . . .	21
16	3D Model of the Tissue Roll . . . . .	22
17	3D Model of the Clock Tower . . . . .	23
18	3D Model of Metate Arch . . . . .	24
19	Finite Element Mesh of Metate Arch . . . . .	25
20	3D Model of Dilitant Fault . . . . .	27
21	Sparse Point Cloud with Mis-located Segment . . . . .	28
22	Repaired 3D Surface Model of Metate Arch . . . . .	29
23	Measurement of Column Diameter of Metate Arch . . . . .	31
24	Plot of Natural Frequencies of First ten Modes in Respect to Approximate Element Size – Metate Arch . . . . .	34
25	Stress and Displacement at the Geometric Centroid of the Section with the Smallest Area with Different FE Meshes - Metate Arch . . . . .	35

26	Plot of Stress and Displacement at the Geometric Centroid of the Section with the Smallest Area in Respect to the Inverse of Approximate Element Size – Metate Arch . . . . .	37
27	Plot of Natural Frequencies of First ten Modes in Respect to Approximate Element Size – Dilitant Fault . . . . .	38
28	Plot of Stress and Displacement Anywhere in the Model in Respect to the Inverse of Approximate Element Size – Dilitant Fault . . . . .	39
29	Region with highest stresses in the Dilitant Fault with Meshes of Different Element Sizes . . . . .	45
30	Region with largest deformation in the Dilitant Fault with Meshes of Different Element Sizes . . . . .	46



## LIST OF TABLES

1	Summary of Imaged Systems . . . . .	6
2	Input Variables for Analysis . . . . .	33
3	Table of Natural Frequencies of First ten Modes in Respect to Approximate Element Size – Metate Arch . . . . .	34
4	Stress and Displacement at the Geometric Centroid of the Section with the Smallest Area with Different FE Meshes - Metate Arch . . . . .	36
5	Table of Natural Frequencies of First ten Modes in Respect to Approximate Element Size – Dilitant Fault . . . . .	37
6	Maximum Stress and Displacement Everywhere in Dilitant Fault with Differ- ent FE Meshes . . . . .	38

# 1 INTRODUCTION AND LITERATURE REVIEW

## 1.1 Overview

The finite element method (FEM) is currently the most prevalent tool for structural analysis in computational mechanics. It is a result of its excellent accuracy of approximation and its comprehensive compatibility with different geometries of structures when analytical solutions cannot be obtained. For structures with irregular geometries, the application of the finite element method might not be constrained only by the analytical solution itself but also the high-cost and inefficiency of modeling to obtain nodal coordinates and the connectivity of elements since they are the essential parts of FEM. A low-cost and user-friendly approach to improve the process of reconstructing 3D models when using FEM for structures with irregular geometries would provide numerous benefits, which also leads to the objective of the present work.

Geometries are required to be established before discretization in FEM. In a typical finite element software package, models of structures with simple geometries can be manually drawn as simplified 1D or 2D objects or directly as 3D objects with the help of drawing tools embedded in the software. If the geometries of the required models are complex, it can be comparatively easier to build the models in a computer-aided design program specifically for building 3D models then have them imported into the finite element package software for structural analysis. However, when the geometries of the structures become more irregular, especially for those of structures with varying curvatures on the surface in all three orthogonal spatial directions, manually establishing accurate 3D models can be technically challenging and strenuous for engineers even with the help of computer-aided design programs. Good examples of such structures and two geometries considered in this work could be natural rock structures like Metate Arch in Devil's Garden and the metal sculpture, Dilatant Fault, at Colorado State University. They are shown in Figure 1.



(a)



(b)

Figure 1: (a) Metate Arch at Devil's Garden, Utah; (b) Dilitant Fault in Colorado State University, Colorado

There are challenges in the perspective of efficient measurement of the structures and establishment of the models, as well as the perspective of budget and technical personnel in the process of manual reconstruction of irregular 3D models. First, the physical dimensions of the structures need to be measured accurately. Even though some general measurements could be completed on site, it is still difficult for technical personnel to measure the local curvatures of points in all three orthogonal directions throughout the surface of the structure since they almost vary at any point on the surface. As a consequence, the on-site measurement process itself can dramatically increase the budget and time prior to the establishment of the 3D model. Second, a model with irregular surfaces would take significant effort for drafting personnel to build accurately in the 3D environment even if the physical dimensions are provided since the curvature at each point on the surface of the structure requires high-level 3D drawing skills to be reflected correctly. Since the majority of the structures are “regular” structures in the sense that they originate with drawings or design plans, it would not be cost-efficient to require the technical staff to possess a high level of 3D drawing skills. Finally, even when the result of manual reconstruction is ideal, the use of traditional methods would cause the budget and time of the reconstruction process to be excessively large.

## 1.2 Literature Review

The advance in the field of photogrammetry has supported many disciplines in the recent years with its prominent advantages in model reconstruction, such as surveying (Westoby et al., 2012; Irschara et al., 2009), topographic mapping (Ameri and Fritsch, 2000; Hugenholtz et al., 2013), rock engineering (Reid and Harrison, 2000; Firpo et al., 2011), cultural heritage (Remondino, 2011; Koutsoudis et al., 2014), environmental research (Ryan et al., 2015), and clinical research (Clement et al., 2004). Photogrammetry provides a user-friendly and low-cost solution for reconstruction of 3D models simply using static 2D photograph sequences taken around the targeted object without using expensive assets and equipment. In structural inspection, photogrammetry has been used to model the structures or measure the displacements of bridges.

### 1.2.1 Surveying

The significant advantage of adopting photogrammetry in topographic surveying is that it employs the automatic camera pose estimation to skip the requirement for manual setup of the control points prior to the acquirement of the photo sequences to shorten the measurement time as compared to traditional methods like terrestrial laser scanning (TLS), differential GPS, or robotic total station (Westoby et al., 2012). The photogrammetric programs can align the photos merely based on the pairing of the spots with similar texture and color of the surface in multiple images, which are used similarly to natural control points (Irschara et al., 2009).

The cost of equipment also drops dramatically since one common commercial camera can be the only physical device that is required. This is in contrast to other methods like TLS, differential GPS, or robotic total station that need to purchase costly sophisticated facilities or contract with a third party (Westoby et al., 2012). The advantages above of low-cost and easy-setup also apply to the reconstruction of 3D models for FEM.

### 1.2.2 Topographic Mapping

Ameri and Fritsch (Ameri and Fritsch, 2000) used only satellite images to reconstruct 3D models of plane-roof structures. If these images can be used combined with a

close-range photo sequence in 360 degrees, the quality and accuracy of the models could be dramatically improved. Photogrammetry is also a prerequisite of small unmanned aircraft system (sUAS) to generate low-cost digital terrain model (DTM) in topographic mapping and geomorphic feature detection (Hugenholtz et al., 2013).

### 1.2.3 Structural Engineering

In the application of structural inspection, the data collected at the scene can require interpretation or be overwhelming in quantity. It can also be difficult to keep the historical record of the inspection (Lattanzi and Miller, 2013). Easy access to modeling using photogrammetry can improve structural inspection by providing detailed data from the scene and record them easily and visually. Bridge inspection using 3D scene reconstruction by photogrammetry was found to be adaptive to complex field scenarios in structural inspection, and the accuracy of the application of photogrammetry is feasible with an average of 8 percent linear distance error, compared with tape measurements (Lattanzi and Miller, 2015). Photogrammetry has also been used to improve the accuracy of the location of voussoirs in a masonry arch bridge (Riveiro et al., 2011). In Riveiro et al.'s study, the individual 3D model of each voussoir is extruded separately from the 2D surface on the exposed side of the voussoir and then analyzed as a group of connected individual members with FEM.

Photogrammetry has been proven to be an efficient and low-cost method to acquire the structural information with high accuracy in bridge deformation and monitoring (Jiang et al., 2008). According to Jiang's research, the amount of time spending on fieldwork with the photogrammetric method can be half of the conventional surveying in bridge geometric measurement. The advantage of monitoring 3D deformation of specimens for laboratory material testing with photogrammetry has also been investigated (Lattanzi and Miller, 2015).

3D Model construction using laser scanning has been researched to acquire the geometry of a bridge for FE analysis for the purpose of health monitoring of bridges (Conde-Carnero et al., 2015; Park et al., 2007). The 3D modeling process in Conde-Carnero

et al.'s study can potentially be achieved using the 2D imaging method discussed in this thesis to improve cost-efficiency.

Possibly because bridges can be made of more than a single material and have joints in the structure, FE analysis of structures adopting only 3D photogrammetry has not been found according to the author's research. With the help of ground penetrating radar to detect the internal construction, a historic bridge was successfully modeled and analyzed using laser scanning and FEM (Lubowiecka et al., 2009). If possible, detection of the internal construction of systems can be used together with photogrammetry to improve the accuracy of results from the FE analysis.

A complete process of FE analysis using 3D models constructed with photos of systems to the author's knowledge has not been explicitly introduced before. With the advantage of photogrammetry, a robust method to utilize it to reconstruct 3D models in FEM for a whole structure is imperative to be developed.

## 2 METHODS

### 2.1 Introduction

Several structural systems were imaged in this study. Four systems were successfully modeled while others were attempted without success. A list of investigated systems, purpose of investigation, result and possible reasons for failures are shown in Table 1. 3D models of the imaged systems are shown in Figure 3.

Table 1: Summary of Imaged Systems

System	Location	Purpose	Result
Highway Guardrail	I25, Colorado	Early imaging attempt	Failure due to the poor light condition
Newton's Corner	Colorado State University	Early imaging attempt	Failure due to its reflective surface
Coffee Mug	-	Investigation	Failure due to its reflective surface
Tissue Roll	-	Investigation	Success
Clock Tower	Colorado State University	FEA Model	Success
Metate Arch	Utah	Complete Analysis	Success
Dilitant Fault	Colorado State University	Complete Analysis	Success

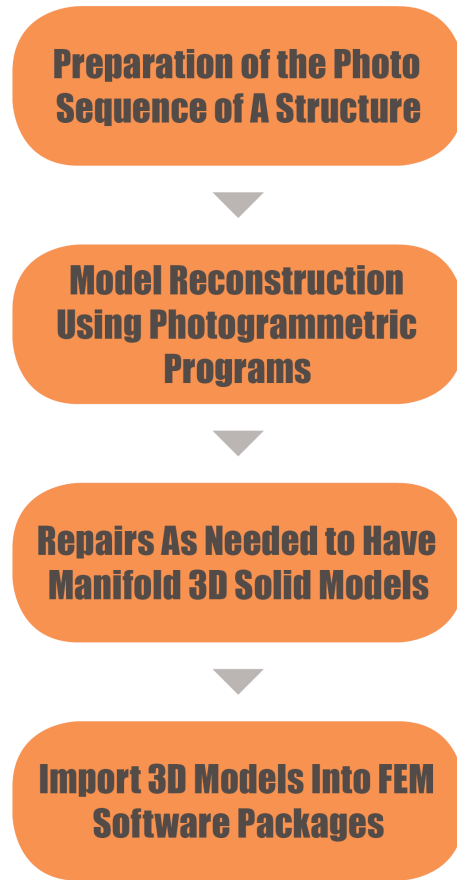


Figure 2: Flowchart of Method Used in this Thesis



Figure 3: 3D Models of Imaged Systems. Clockwise from upper-left: a highway guardrail, Newton's Corner, a coffee mug, a tissue roll, Metate Arch, Dilatant Fault, the clock tower.



## 2.2 Preparation of Photo Sequence

A sequence of photos that captures most surface of a structure needs to be properly prepared following some general rules to achieve successful model construction in photogrammetric programs. Many photogrammetric programs are available such as Agisoft PhotoScan (Agisoft LLC, 2011), VisualSFM (Wu et al., 2011; Wu, 2013) and Bundler (Snavely et al., 2006). Agisoft PhotoScan was used in this study.

The application of photogrammetry in constructing finite element meshes follows many steps for other applications. General guidance for taking photo sequences for 3D model construction in Agisoft PhotoScan can be found in Agisoft PhotoScan User Manual (Agisoft LLC, 2011). Only those additional steps necessary for model construction for FEM will be discussed in detail. Since not all of the structures are suitable for using photogrammetry to construct the 3D models, recommendations for choosing applicable structures and preparation of photo sequences are discussed within this section.

### 2.2.1 Details of Surface

Details on the surface of structures are the main source of natural control points for photogrammetric programs to properly align photos and sketch the geometry of target structures (Westoby et al., 2012). The success of photo alignment is directly related to the surface detail of the structure (see Section 2.3). Good surface details for photo alignment can be either the physical unevenness of the surface or the visual texture of the material of the structure.

Without sufficient surface details, photogrammetric programs might not be able to determine the locations of cameras due to lack of control points. Location of an area on the surface can be uncertain in the 3D coordinates if the relative locations of the control points within the area are uncertain. A good analogy would be a 2D drawing of a cube without details, such as shading, where it can be impossible to determine the direction of the cube, as shown in Figure 4. Therefore, a lack of surface detail can lead to insufficient or even no control points for certain areas on the structure. Accordingly, the photos associated with these areas may not be properly aligned.

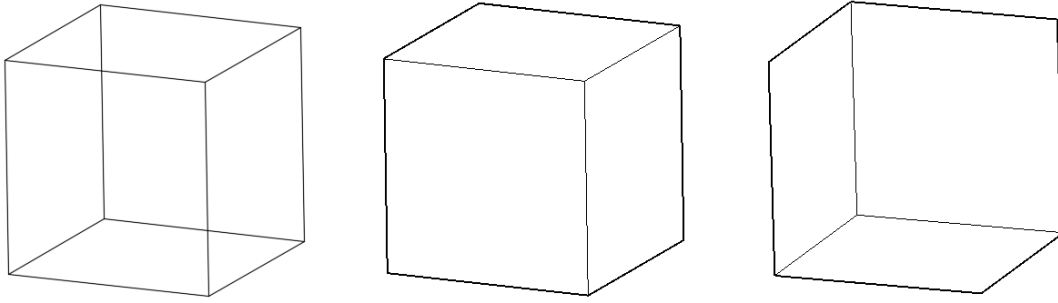


Figure 4: 2D drawing of a 3D object without sufficient details can poorly indicate its direction. (a) 2D image showing only the edges of the object; (b) one interpretation of the object in 3D; (c) the other interpretation of the object in 3D.

### 2.2.2 Reflective Surfaces

If an area on the surface of a structure is showing different colors in a photo sequence, it cannot be considered as a legitimate region to model during photo alignment process. A reflective surface can cause the surface facing directly to the position of the camera to be brighter than adjacent areas. One area on the structure can be rather bright in one photo but appears to be much dimmer in another (Agisoft LLC, 2011). Therefore, reflective surfaces are not legitimate to be modeled in photogrammetric programs. An example would be if a sequence of photos of a mirror is analyzed by the program, it is more likely that the reflected scene would be modeled rather than the surface of the mirror. This can also be the main reason causing the failure of model construction for Newton's Corner.

### 2.2.3 Lighting Condition

If the brightness varies significantly along the surface of the structure, the positions of the cameras might not be located accurately by the imaging tools. The area with dimmer light might be shown as discontinuous in the sparse point cloud. Sparse point cloud in Agisoft PhotoScan contains the control points to roughly locate the objects in a 3D coordinates. This effect can be magnified and cause large holes in the 3D surface model if the structure has a concaved segment that receives even less light. As a result, it is recommended to have ambient light at the scene to reduce the variation of lighting

at different sides of the structure (Agisoft LLC, 2011). In Figure 12, the guardrail was not aligned successfully most likely to poor lighting conditions.

#### 2.2.4 Overlap

An overlap of 60 percent of the surface between photo to photo is suggested (Agisoft LLC, 2011). 30-degree elevation of angles was also recommended when acquiring photos from above a structure (Morgan et al., 2017). Without sufficient overlap, Agisoft PhotoScan may not successfully determine the positions of cameras due to lack of relative control points.

#### 2.2.5 Targets

When the sparse point cloud is inaccurate or a significant number of the photos are not aligned, it might be a sign of a lack of surface details on the structure. In this case, targets can be placed around the structure when the photos are taken (Morgan et al., 2017). Figure 5 contains some of the different targets provided by Agisoft PhotoScan which can be printed out and placed at the scene. The purpose of using these targets is to improve photo alignment by providing additional, easily recognizable control points in the photo sequence. This cannot guarantee the quality of the sparse point cloud if there are other issues such as reflective surfaces with the surface of the structure. Targets were used when modeling the coffee mug, which is discussed in section 2.4.3.

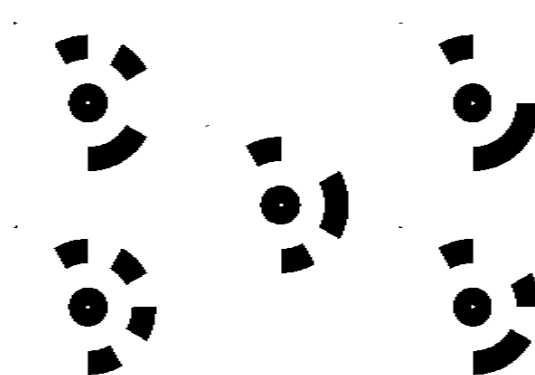


Figure 5: Printable Targets Provided by Agisoft PhotoScan

## 2.3 Use of Photogrammetric Software

### 2.3.1 Photo Alignment

A sequence of photos covering the surface of most structures can be imported into Agisoft PhotoScan to construct the 3D model. Each photo in the sequence is analyzed by the program to determine the position of the camera. After the positions are determined, the photo alignment process is complete and the location of the system in a 3D coordinate is roughly sketched using a sequence of points called a point cloud.

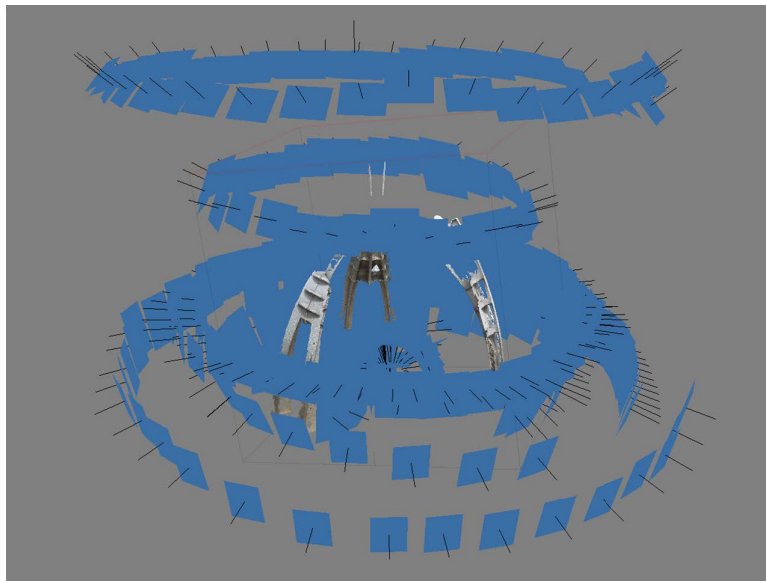


Figure 6: Positions of cameras of aligned photos are demonstrated as the blue rectangles in the 3D model of Newton's Corner in Agisoft PhotoScan.

A single point in the 3D coordinate is determined by pairing this point on the photos taken from different angles, in which the points in different photos are chosen based on their identical color and the relative location of the point to other points (Irschara et al., 2009). The collection of these paired points in a 3D coordinates is defined as a sparse point cloud. When an adequate number of points are paired, the positions of the cameras associated with these points are also determined. Figure 6 shows that the positions of the cameras are demonstrated as blue rectangles in the Agisoft PhotoScan.

The sparse point cloud directly reflects the general shape of the object and it is also relevant to the position of the camera. If the position of the camera of a photo is dislocated

in the 3D coordinates, then the sparse points that are associated with this photo might be inaccurate as well. For example, part of the sparse point cloud in Figure 15 resulted in constructing an extra handle of the mug.

Trimming inaccurate points in the program when alignment is performed can reduce the amount of inaccurate dense points being created (Agisoft LLC, 2011). It may be interpreted thus: by deleting the sparse points that are associated with a dislocated picture, it can reduce the participation of this dislocated picture in the process of generating the dense point cloud, and thereby improve the accuracy of the model construction.

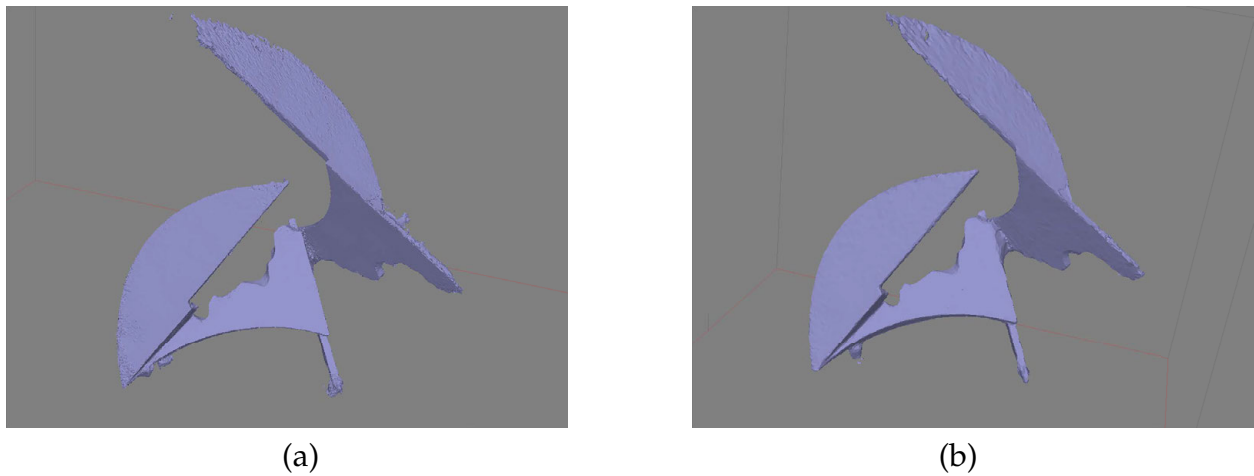


Figure 7: Contrast of options with and without modification of sparse point cloud. (a) The surface model without the modification is comparatively rough; (b) the surface model with the modification is cleaner and more close to the actual structure.

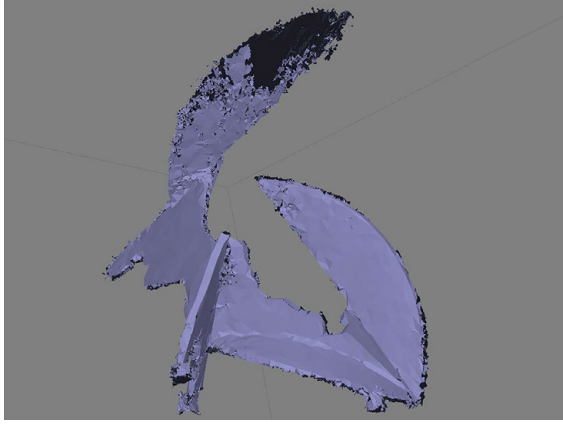
Limiting the control points in the settings of the photo alignment process determines the maximum number of sparse points to be generated during the photo alignment process. Increasing the limit of control points can enable access to more sparse points to be verified and edited and helps in improving the accuracy of the dense point cloud which is generated based on the sparse cloud. Figure 7 shows the comparison between two 3D surface models that were constructed with and without editing of the inaccurate points in the sparse point cloud.

### 2.3.2 Model Construction

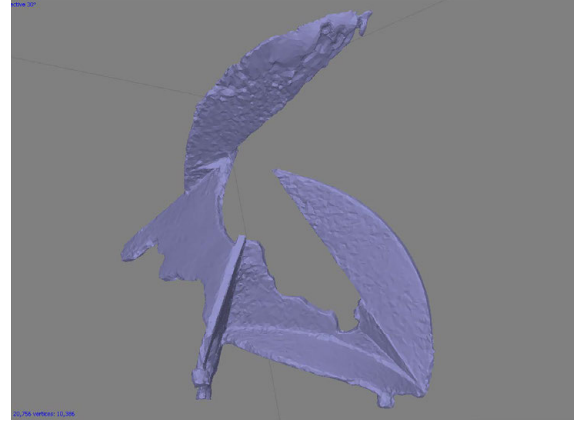
Creating the dense point cloud is an important process if a good quality of the 3D surface model is desired, especially for structures with complicated geometries. A 3D surface model is generally a collection of multiple individual triangular planes formed by connecting points in the point cloud. As the number of points increases, the point cloud is more likely to have individual planes that are intersecting each other, which can cause issues for the later on processes.

Agisoft PhotoScan provides two methods to improve the continuity of 3D surface model. Under the interpolation mode, additional planes are inserted in the gap between surfaces with a small difference of radii. Holes are still expected to be present at gaps with sharp angles or in areas without enough points. Under extrapolation mode, the program projects the edges of the gaps and tends to close any gaps regardless of radii of the surface. The approximation of the surface in the gap might not be accurate if dense points are insufficient to provide the guidance of the projection (Agisoft LLC, 2011). If neither of these two methods is used, the holes in the 3D surface model can be prevalent, and it may lead to additional repair or even irreparable holes. Figure 8 shows the holes in the 3D surface model without interpolation as well as bulged areas under interpolation mode.

If fewer individual planes are desired to have only the general layout of the structure, the parameter of maximum faces in the model construction process can be used to limit the number of the individual planes by integrating detail surfaces (as shown in Figure 9). After the 3D surface model is constructed based on the dense point cloud, the texture of the model can be built in Agisoft PhotoScan. 3D surface models without and with the texture can be seen in Figure 20 (b) & (c), accordingly.

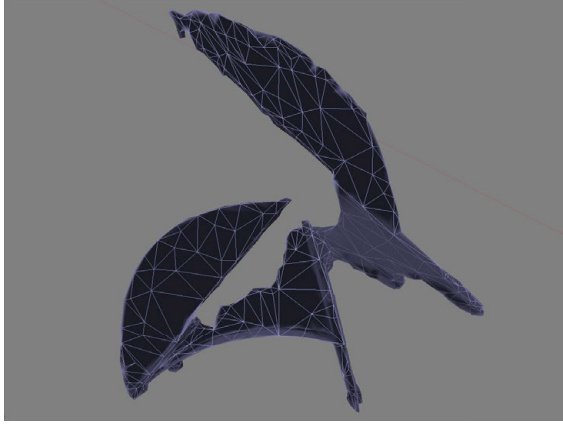


(a)

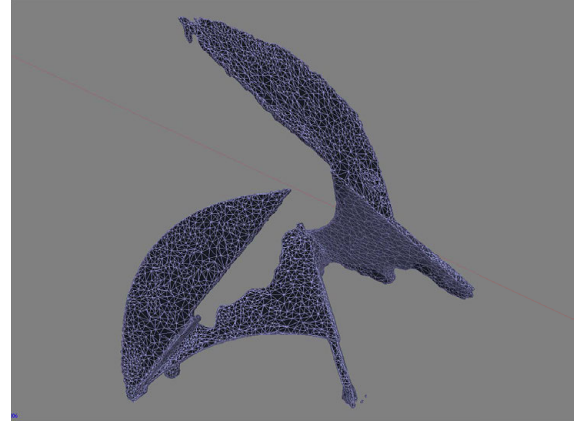


(b)

Figure 8: Contrast of 3D Surface Model with Interpolation. (a) surface model constructed without using interpolation; (b) surface model constructed using interpolation.



(a)



(b)

Figure 9: Example of 3D Surface Models with Different Numbers of Faces. (a) 3D surface model with 2,000 faces; (b) 3D surface model with 20,000 faces.

### 2.3.3 Masking

Masking of photos is a process to exclude the irrelevant objects in the photos to isolate the target structure from the background during photo alignment. An example of using mask is shown in Figure 13 (b). After the 3D surface model is constructed, masks for the photo sequence can be automatically created by Agisoft PhotoScan based on the constructed model.

Masking of photos can help to eliminate the distractions from the background in photo alignment process. This process can greatly improve the quality of the alignment if

the background provides similar pattern or color to the surface of the target structure. If a 3D surface model has coarse edges, using masks for the second phase of model construction can improve the smoothness along the edges. A comparison of whether or not using masks can be seen in Figure 10. In this example, the background in the photo sequence consists of the pure blue sky. Objects like this appear to be the same in any direction thus it can confuse the program. The program will be unable to determine the actual location of the blue object on the 3D coordinates, which can increase the chance for the sky to be interpreted as objects on the edges of the structure.



Figure 10: Contrast of 3D Surface Models Constructed with Masks of Photos. (a) 3D surface model constructed with regular photos; (b) 3D surface model constructed with masked photos.

#### 2.3.4 Manifold Solid Model

3D surface models constructed by Agisoft PhotoScan typically cannot be directly used in FEM analysis packages. Abaqus CAE requires the imported model to be a 3D solid that is able to be assigned with volume and weight. These 3D solids are called manifold 3D solids. 3D models directly constructed by Agisoft PhotoScan are only individual triangular 3D surfaces. The 3D surface can be transformed into 3D solid by many programs, but first, they need to be a manifold 3D surface, also known as the watertight 3D surface. Manifold 3D surface is defined as a 3D surface that encloses itself and does not have any gaps and self-intersection. Therefore, to ensure that the 3D surface model can be transformed into 3D solid, any holes in the 3D surface model need to be closed.



In Agisoft PhotoScan, the Close Hole tool (see Figure 11) can be used to repair the continuity issue in the 3D surface model. However, some holes may not be fixed by this tool if there are self-intersected surfaces. This is more likely to happen when the 3D surface model is constructed based on a dense point cloud with too many points. As a result, it may be better to reduce the size of the dense point cloud to prevent surface intersection. If the non-manifold issue still cannot be resolved in the photogrammetric programs, the further repair will be needed in other 3D modeling programs.

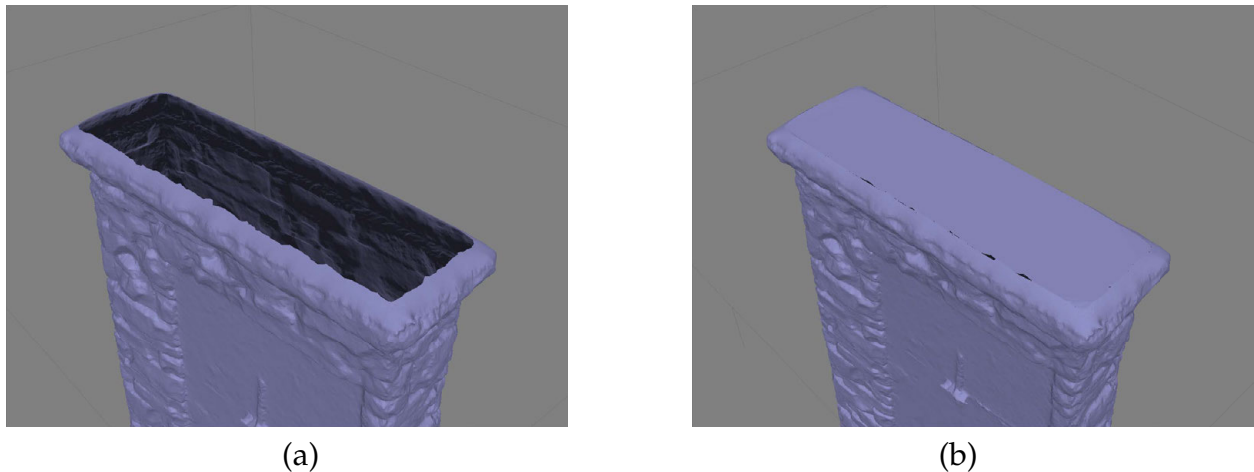


Figure 11: Example of Using Close Hole Tool in Agisoft PhotoScan. (a) hole on the top of the 3D surface model; (b) the hole is closed.

## 2.4 Imaging of Systems

### 2.4.1 Highway Guardrail

A highway guardrail at Exit 268 of I25, Colorado, was attempted to be constructed with finite element mesh. Three sets of photos with 690, 904 and 1177 images were taken successively. None of these sequences was successfully aligned, possibly due to the poor light condition and lack of surface detail.

Figure 12 (a) & (b) show the distinct contrast of brightness in two different sides of the guardrail. The guardrail itself has some areas where the sunlight can not penetrate. Surface details on the alloy stem can be hard to collect due to the monochrome material. The cap of the guardrail in the actual photo and 3D surface model can be seen in Figure

12 (c) and (d). The 3D surface model with discontinuous segments is shown in Figure 12 (e). This poor image might be caused by the monochrome material of the guardrail cap.



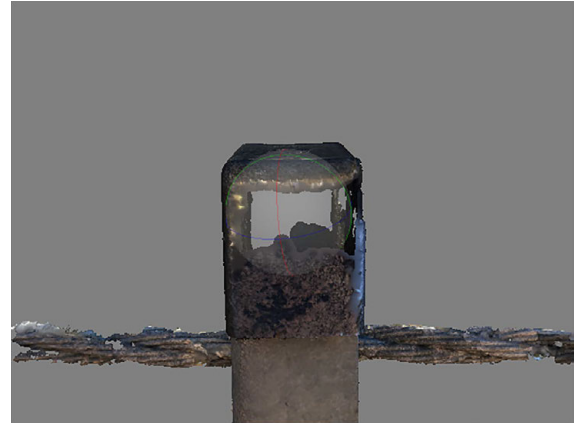
(a)



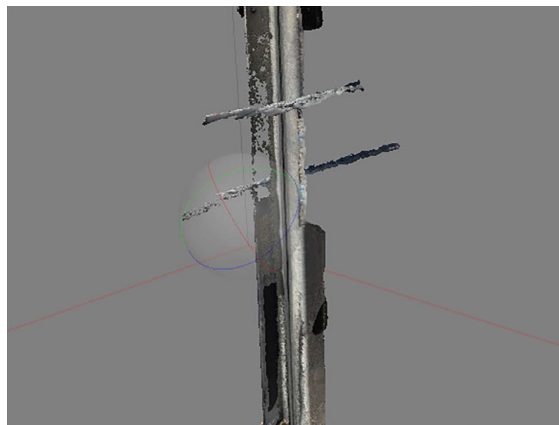
(b)



(c)



(d)



(e)

Figure 12: (a) & (b) Contrast between photos of brighter and dimmer side of the guardrail; (c) the cap of the guardrail ; (d) segment of the guardrail cap is completely missing; (e) main body of the guardrail is discontinuous.

### 2.4.2 Newton's Corner

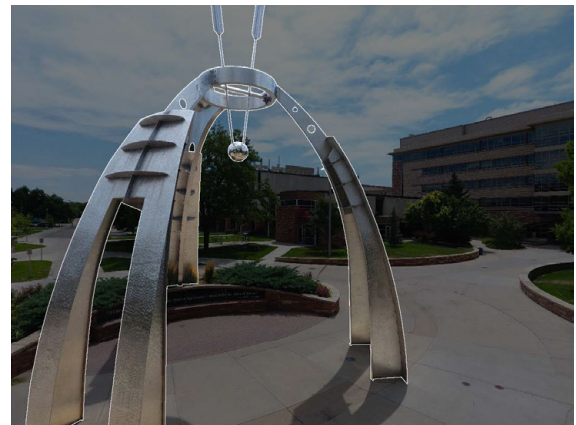
Newton's corner, as shown in Figure 13 (a), is a landmark sculpture at Colorado State University. An unmanned drone, DJI Phantom 4, was piloted to take photos from above of this 40 feet tall structure to cover the top part of the structure.

Masks of photos were manually sketched in Agisoft PhotoScan to exclude the background in the photo sequence for the second attempt of the model construction. The shaded area in Figure 13 (b) is an example of a masked photo in Agisoft PhotoScan. With these masks, the background of 335 photos of Newton's Corner would be neglected during photo alignment, and the sparse point cloud will not include the points from the background. Use of masks is introduced earlier in Section 2.3.3.

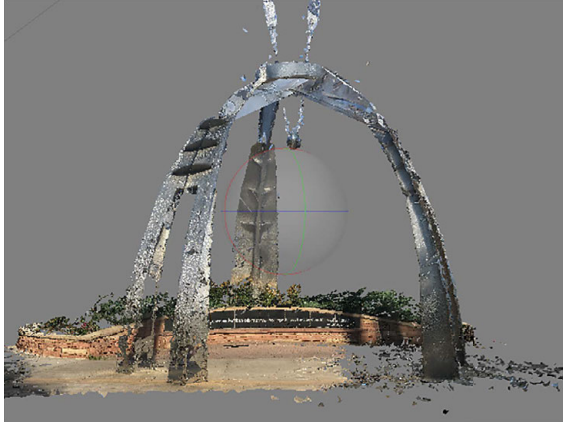
The first model constructed has many broken pieces and it is shown in Figure 13 (c) and (d). The failure of the model construction of Newton's Corner can be attributed to its reflective surface. As a result, the second phase of model construction in Agisoft PhotoScan did not provide an ideal result although masks of photos were used. The areas on the structure under direct sunlight still contained a large number of inaccurate sparse points during the model construction. Clean edges correctly reflect the actual geometry of the structure that could barely be seen in these areas. The 3D model constructing using masks is shown in Figure 13 (e).



(a)



(b)



(c)



(d)



(e)

Figure 13: (a) Newton's Corner; (b) masked photo in Agisoft PhotoScan; (c) first attempt of model construction without using masks; (d) a close look at one "broken leg" of the Newton's Corner model; (e) the second attempt of model construction using masks.

### 2.4.3 Coffee Mug

The coffee mug shown in Figure 14 (a), was modeled to analyze the effect of the reflective surface on the quality of the 3D surface model. It was poorly modeled for the first attempt as shown in Figure 14 (b). The identical cartoon figure on both front and back of the mug was misinterpreted by the program as they are the same figure. As the result, two handles appear on both sides of the mug while the actual mug only has one handle. In Figure 15 (c), it can be seen that only half of the coffee mug is showing in the model since the one side was merged into the other.





(a)



(b)



(c)



(d)

Figure 14: Models of A Coffee Mug Constructed Using Masks. (a) Coffee mug used to investigate the alignability of objects with reflective surface; (b) 3D surface model of the coffee mug constructed without having distinct background or targets; (c) targets placed at the scene for the second attempt; (d) 3D surface model of the coffee mug with distinct background and targets.

Figure 14 (c) shows that the targets were used to improve the alignment of the photos. Compared with the 3D model constructed without targets in Figure 14 (b), the model in Figure 14 (d) is much better aligned when targets were used. The other half of the mug was successfully modeled, and only one handle is shown. Unfortunately, since the targets cannot compensate the monochrome and reflective surface of the mug, the 3D model of the coffee mug was still incomplete.

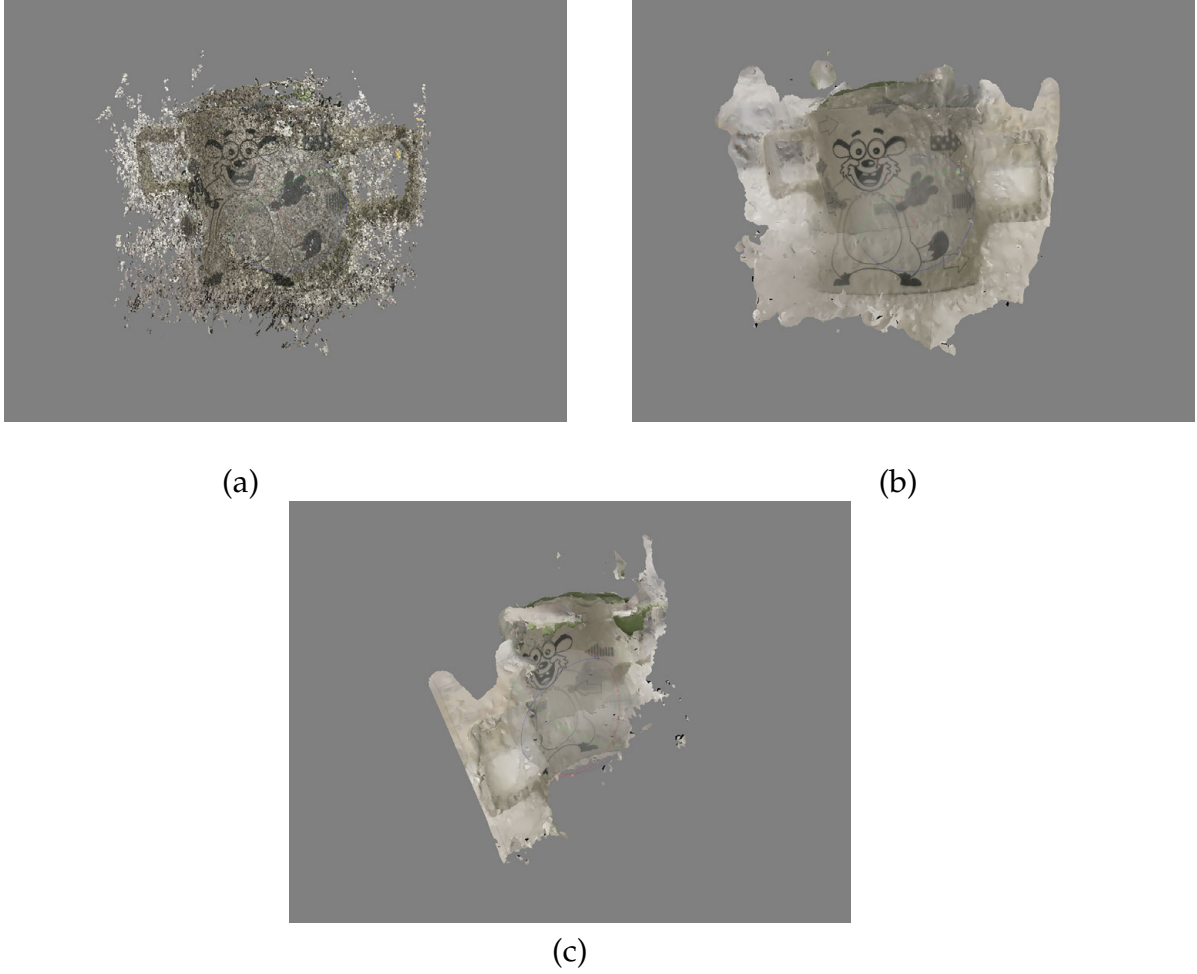


Figure 15: Example of A Poor-Quality 3D Surface Model. (a) dense point cloud with poor quality; (b) a front view of the 3D surface model; (c) a side view of the 3D surface model.

#### 2.4.4 Tissue Roll

A tissue roll was used to compare with the result of the coffee mug to determine whether the unsuccessful alignment was caused by the reflective surface or the monochrome surface. Despite the monochrome surface of the tissue roll, it was modeled successfully with the distinct pattern and the matte surface. The photos were taken against a background with distinct color without using targets, and the constructed 3D surface model was satisfactory as shown in Figure 17. It can be seen that the inner side of the tissue roll was not modeled completely likely due to insufficient light in the area.

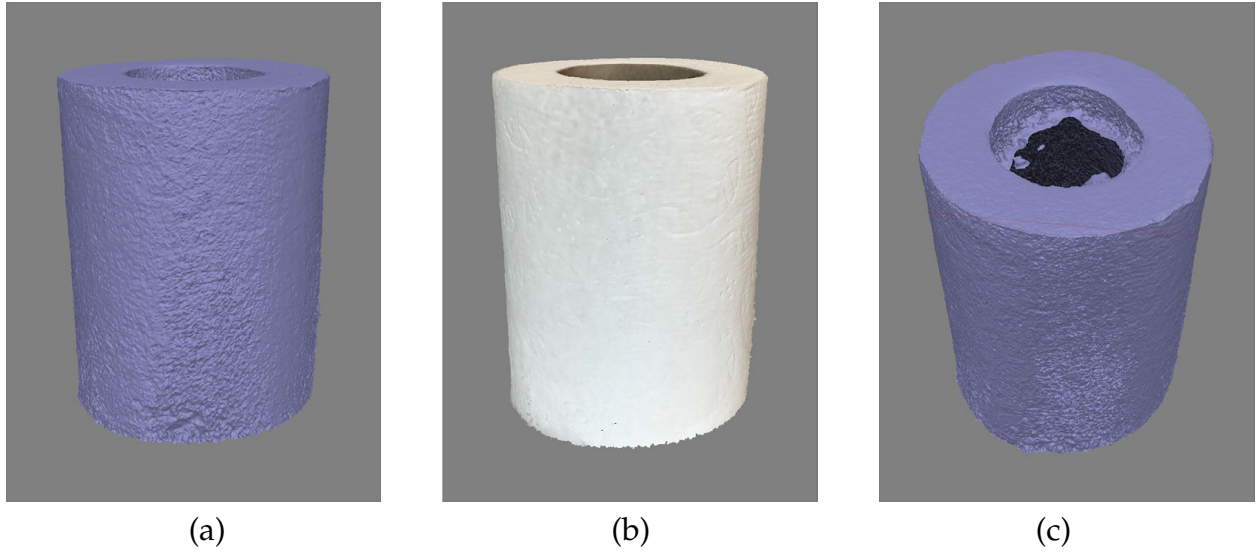


Figure 16: 3D Model of the Tissue Roll. (a) 3D surface model of the tissue roll; (b) surface model of the tissue roll with texture; (c) the inner side of the tissue roll was not modeled completely.

#### 2.4.5 Clock Tower

A clock tower located in front of Engineering Center, Colorado State University and is shown Figure 17 was modeled to investigate the effect of the uneven surface and color variation on the accuracy of photo alignment in Agisoft PhotoScan.

The 3D model of the clock tower was almost flawless and the model was successfully imported into Abaqus CAE, as shown in Figure 17 (e) & (d). Without having many gaps and self-intersection, the 3D surface model was smoothly transformed into a 3D solid and imported into Abaqus CAE.

The photos of the clock tower were taken on a cloudy day to reduce the reflection caused by strong daylight. It also allowed the structure to have an even distribution of light on the surface of the tower. A total of 251 photos of the clock tower were aligned precisely as the dense point cloud was used to construct a 3D surface model without holes in the main body. A very detailed 3D surface model from the model construction can be seen in Figure 17 (d). The Close Hole tool in Agisoft PhotoScan was used to close the hole at the top of the clock tower since this area was not covered by any of the photos.

The 3D model of the clock tower was successfully constructed and converted into

a compatible 3D part in Abaqus CAE. Although FE analysis of the model was not proceeded due to its relatively less complex geometry.



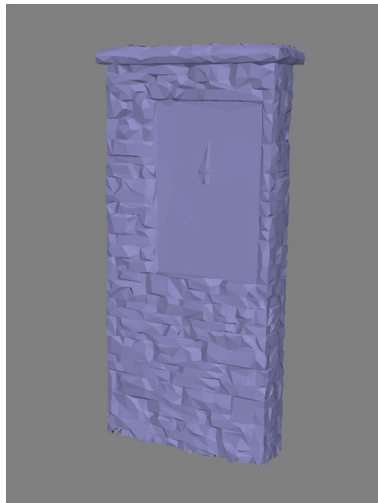
(a)



(b)



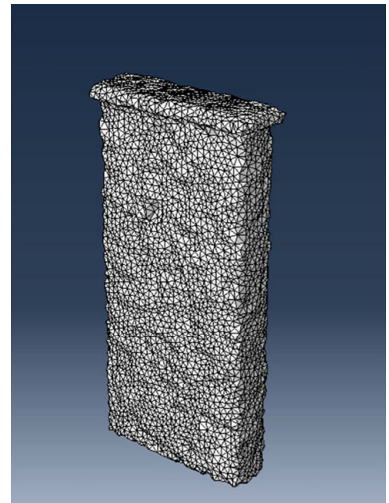
(c)



(d)



(e)



(f)

Figure 17: (a), (b) & (c) The clock tower in front of Engineering Building at Colorado State University, Fort Collins; (d) A surface model of the clock tower; (e) a surface model of the clock tower with texture. (f) 3D model in Abaqus CAE.



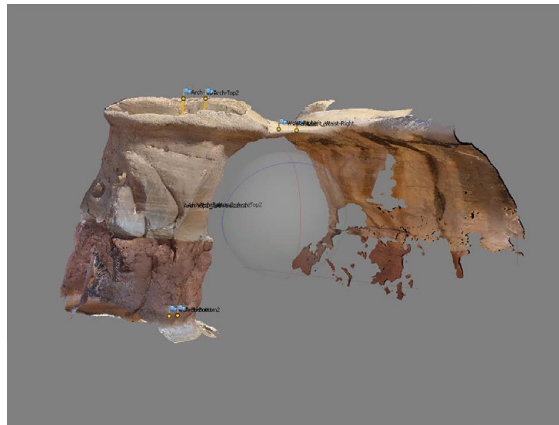
#### 2.4.6 Metate Arch



(a)



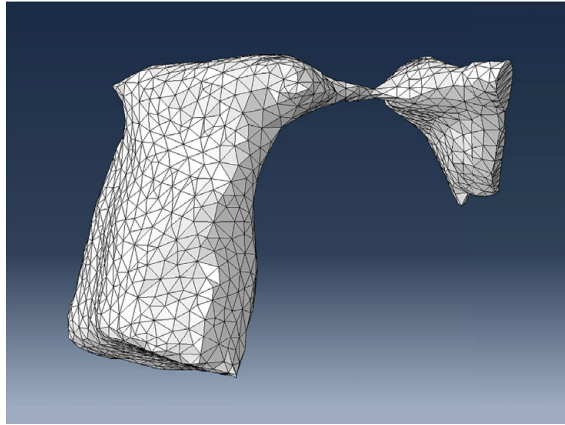
(b)



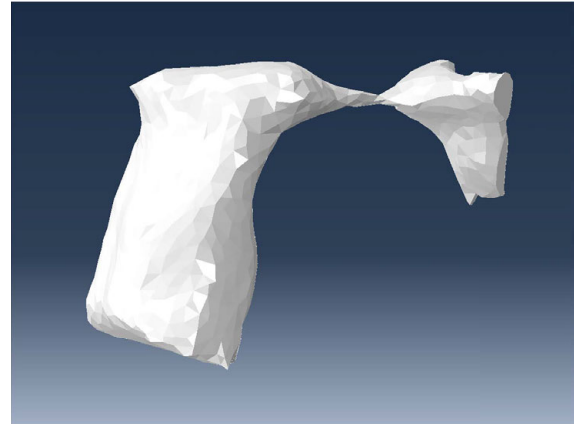
(c)

Figure 18: Model construction of Metate Arch. (a) The side with direct sunlight; (b) The side with shadow; (c) a surface model of the Metate Arch with texture.

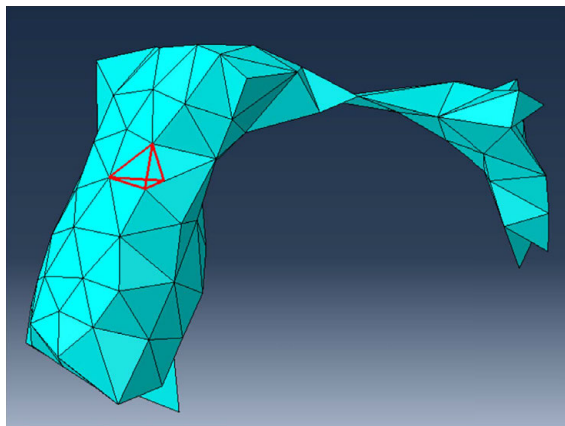
Metate Arch shown in Figure 1 (a) is a rock arch with a narrow section framing into a rock pier on one side and a large volume of rock on the other side. The naturally formed geometry and the homogeneous material of Metate Arch make it an ideal candidate for the application of 3D modeling using photogrammetry. Details on the surface of the caprock can be a good source of control points to benefit the photo alignment in photogrammetric programs.



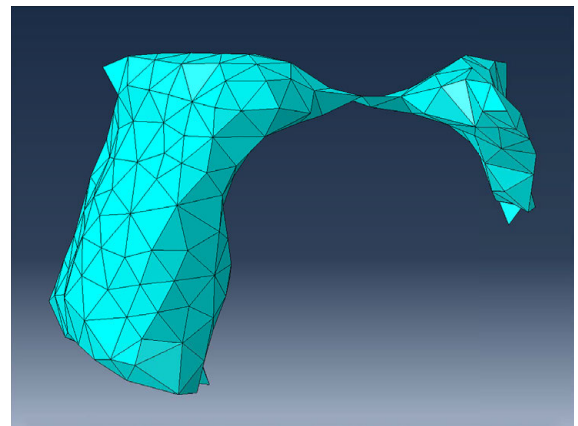
(a)



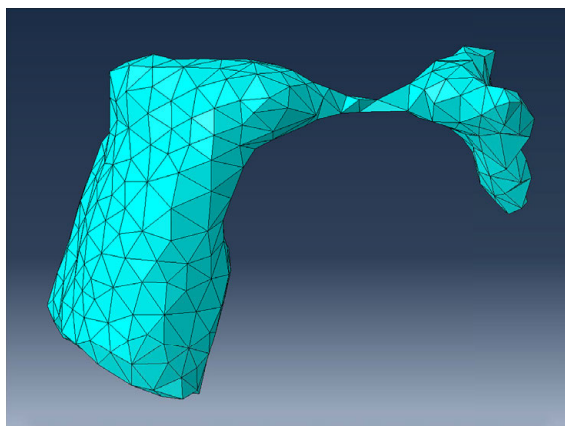
(b)



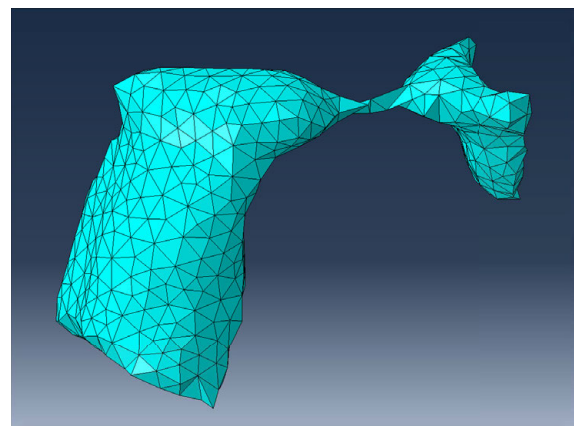
(c)



(d)



(e)



(f)

Figure 19: (a) The 3D solid model imported in Abaqus CAE with virtual topography (black lines); (b) the 3D solid model without virtual topography; (c) a 3D element in the mesh (red tetrahedron); (d), (e) & (f) mesh with different number of elements.

85 out of 91 photos were successfully aligned to construct the model. The unaligned photos can be caused by insufficient overlap with other photos or the color difference between photos due to poor light condition, which is shown in figure 18 (a) and (b). The detailed discussion of the effect of lighting condition can be found in section 2.2.3. The result of the model construction is satisfactory and the most surface of the rock arch is captured as shown in Figure 18 (c).

Figure 19 (a), (b) & (d) shows the model in different stages of the discretization process after it was imported into Abaqus CAE. Discretization is discussed in Section 2.6. Six meshes with different numbers of elements were created. The example comparison among the meshes can be seen in Figure 19 (d), (e) & (f). Results of stresses and deformations at the mid arch for a typical loading are discussed in the Results chapter.

### 2.4.7 Dilitant Fault

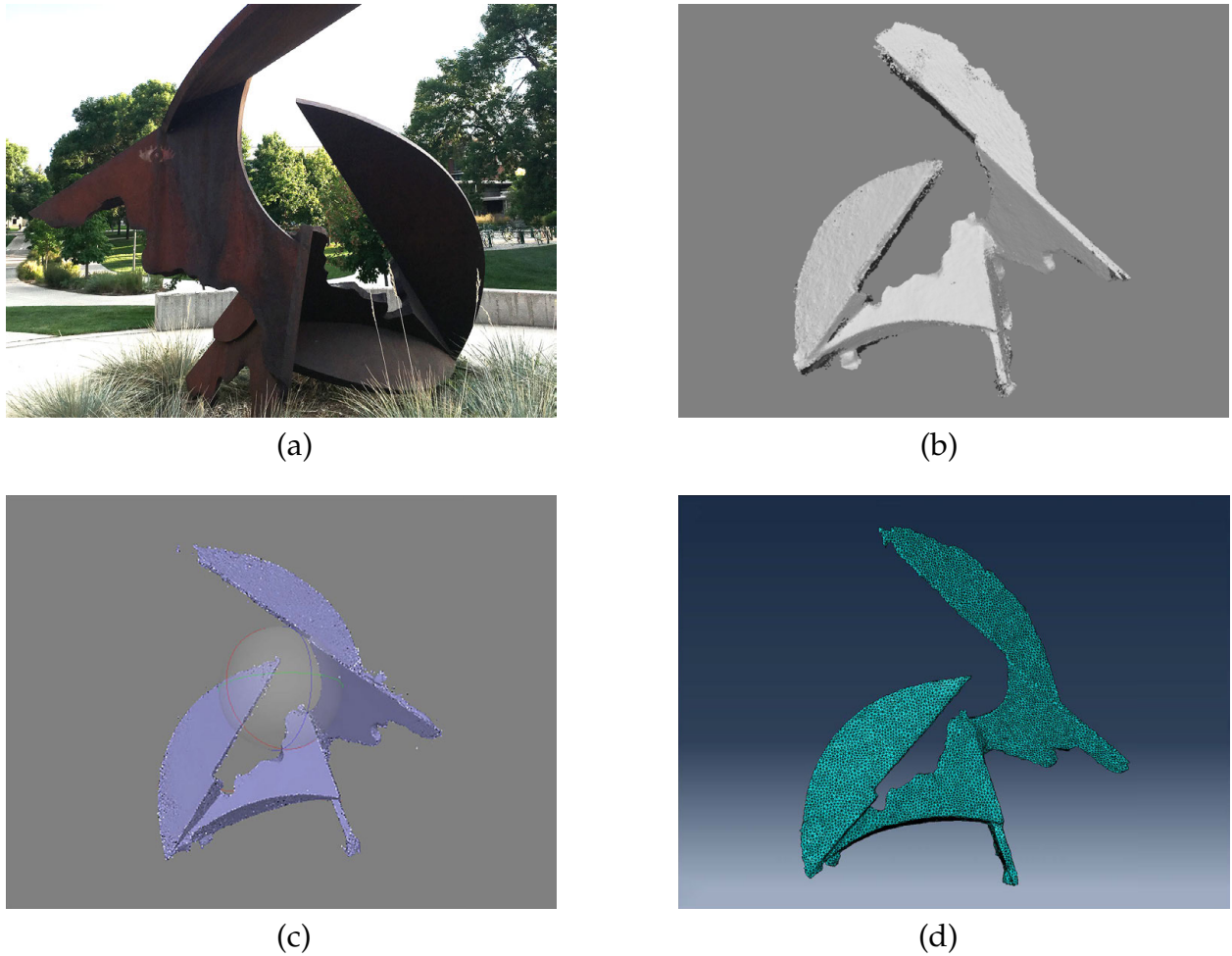


Figure 20: (a) a photo of Dilitant Fault; (b) the sparse point cloud of Dilitant Fault; (c) a surface model of Dilitant Fault; (d) the FEM mesh of the 3D model of Dilitant Fault in Abaqus CAE.

Dilitant Fault is a metal-made sculpture on the campus of Colorado State University (Figure 20 (a) ). 366 of 394 photos were aligned to construct the complex geometry of the sculpture. When acquiring photos of this structure, the challenges are 1) inadequate color variation of the surface and 2) corners and regions at the bottom of the sculpture can be poorly lit under natural conditions because of the upper parts of the sculpture.

Since the color of the sculpture is not completely monochrome, the slight change of color and pattern on the surface helped the alignment of the photos. Several photos were aligned incorrectly during the first attempt and the sparse points associated with

these photos can be easily seen in the sparse point cloud view as shown in Figure 21. In a subsequent attempt, most photos were aligned correctly and a decent 3D surface model was successfully constructed and converted into compatible FE model in Abaqus CAE (Figure 20 (d) ).

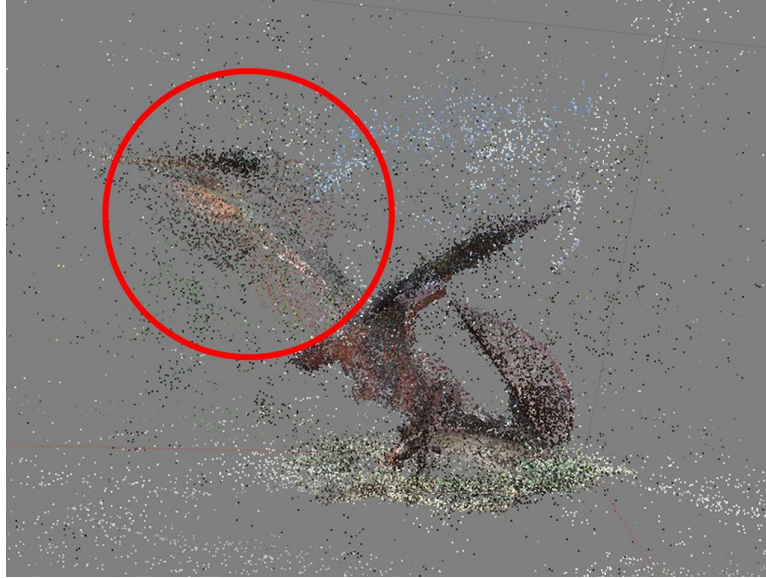
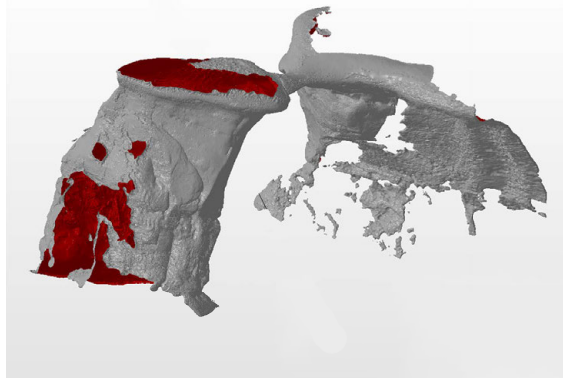


Figure 21: An example of mis-located segment in the sparse points, shown in the 3D model of Dilitant Fault.

## 2.5 Repair for Non-Manifold Model

Repair of non-manifold 3D models after the initial construction of the 3D model is important because it will directly affect whether or not the model is able to be analyzed in FEM software packages. Autodesk NetFabb is an additive manufacturing and design software that supports automatic repair solution for non-manifold 3D models. In this research, Autodesk NetFabb was used to resolve the issues with holes and self-intersection in the 3D surface model of Metate Arch. The model before and after the repair in Autodesk NetFabb is shown In Figure 22.





(a)



(b)

Figure 22: Repaired 3D Surface Model of Metate Arch. (a) The original 3D surface model constructed by Agisoft PhotoScan; (b) the repaired 3D surface model.

Manifold 3D surface models can be transformed into 3D solids in AutoCAD. However, since no mutually supported file format was found between Autodesk NetFabb and AutoCAD, an open source mesh-editing program, Meshlab, was used to convert the model in .stl format into .dxf format for the file to be recognized by AutoCAD.

The .dxf file that exported by MeshLab is in the format of individual polylines. In AutoCAD, these polylines need to be first converted into surfaces using "ConvToSurf" command and then combined into a single surface using "Union" command. After this, a mesh can be created based on the surface, which is a prerequisite for building a solid. "ConvToSolid" command was used to build the solid upon the mesh. After the conversion, the 3D solid model is ready to be exported and then used in FEM software packages. Abaqus CAE supports many file formats for importing parts. In this work, the file format .sat was used to export the 3D solid model of Metate Arch from AutoCAD.

In some cases, either because the model was constructed based on too many dense cloud points, or some of the individual surfaces in the model are too close to each other, the intersection issues in the surface model might not be able to be fixed completely by Autodesk NetFabb. The model might be shown as a manifold 3D surface in Autodesk NetFabb, but it will not be able to be converted to a 3D solid in AutoCAD. Rhinoceros 5 was then found helpful in this situation to efficiently convert the 3D model. Rhinoceros

5 is a versatile 3-D modeler program. In Rhinoceros 5, the command MeshToNURF was used to transform the 3D surface into 3D solid. The command WHAT can also be used to check whether the polysurface model is valid and manifold. If the model is non-manifold, Abaqus CAE will report an error when discretizing the 3D solid. As an example, the model of Dilatant Fault was successfully repaired in Rhinoceros 5.

## 2.6 Discretization

The 3D solid model of Metate Arch was discretized in Abaqus CAE using four-node tetrahedrons. With other types of element shape, the model might not be successfully discretized. The model is a 3D solid without any curved surface since it was transformed from a 3D surface models consisting of many individual triangular planes. All the vertexes and edges of the 3D solid model are based on the geometric mesh of the 3D solid, which was previously the polyline mesh of the 3D surface model. These vertexes and edges are objects separate from the 3D solid model and defined as virtual topography in Abaqus CAE, which can be used as edges to discretize the model. In other words, the size of elements cannot be larger than the existing cells in the virtual topography, and it is more likely to get elements with uneven sizes since the virtual topography controls the minimal edges and mesh seeds in the discretization process.

### 2.6.1 Model Size

3D solid models can be scaled to the actual size of the structure in Abaqus CAE. This can help to provide results that directly reflect the behavior of the structure in reality. The steps below are how Metate Arch was scaled in Abaqus CAE. After the size is adjusted, it is recommended to also rotate the model in the Assembly module to match its direction in reality so that it is easier to specify the direction of the applied loads later on.

1. The rough diameter of the "pillar" of Metate Arch was chosen as the reference to scale the model. The diameter was approximated to be 4.5 m based on visual inspection of the photo sequence.
2. The diameter of the column in the 3D solid model was were measured to be

2.166 (m). Two nodes used to evaluate the diameter and the magnitude of the distance are shown in Figure 23.

3. The ratio of the actual diameter of the column to that of the 3D solid model was used to scale the model. The ratio for Metate Arch is  $4.5\text{m}/2.166(\text{m}) = 2.08$ .

4. When discretizing the scaled 3D solid model, the approximate element size was also adjusted to match the scaled size.

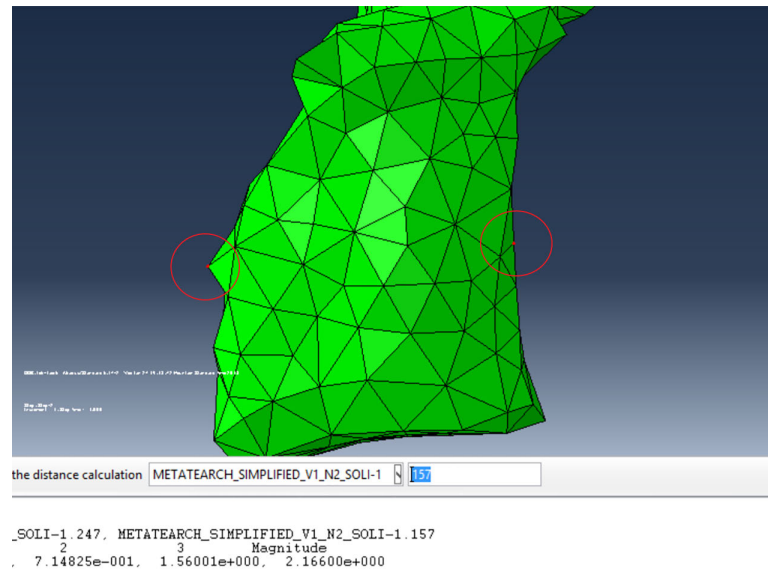


Figure 23: Measurement of Column Diameter of Metate Arch

## 2.6.2 Removing Virtual Topography

To discretize the model with flexible and even sizes of elements, the virtual topography needs to be removed before the discretization by using the tool Combine Virtual Topography. Since boundary conditions and loads can only be assigned at vertexes and edges, some of them might need to be restored using tool Restore Virtual Topography. The vertexes and edges are the baselines for discretization, thus the existing element mesh will be deleted in Abaqus CAE when restoring vertexes and edges. As the result, the efficient procedure to keep the smooth workflow of the discretization would be 1) remove virtual topography, 2) restore desired vertexes and edges, and 3) create the element mesh.



### 2.6.3 Mesh Size

During the discretization process, the approximate size of the element controls the targeted overall size of the element during discretization. This parameter controls the scale of the element mesh after removal of the virtual topography. In Abaqus CAE, if the model definition is requested to be in the output of the analysis, the nodal coordinates and connectivity of elements will be tabulated in the .inp file within the project folder.

### 3 RESULTS

The natural frequencies of Metate Arch and Dilitant Fault were investigated in this thesis, as well as the stresses and deformation under an applied load. For analyses of both of these two systems, it was presumed that a person is standing on the mid-arch of Metate Arch and top of the Dilitant Fault. Since variables in Abaqus are unitless, input data are kept consistent in the same unit system to validate the unit of the outputs. The values and the corresponding units of the input are listed in Table 2.

Table 2: Input Variables for Analyses

Input	Metate Arch	Dilitant Fault	Unit
Elastic Modulus, $E$	10,000,000,000	200,000,000,000	Pa
Poisson Ratio, $\nu$	0.195	0.3	-
Density, $\rho$	2710	8050	kg/m <sup>3</sup>
Load, $P$	750	750	N

The material properties and the applied load are presumed based on the following information:

- The typical elastic modulus of the sandstone is between 10 to 20 GPa. A value of 10 GPa is used in the analysis of Metate Arch to account for a conservative analysis. The material of the Dilitant Fault is assumed to be steel and have an elastic modulus of 200 GPa.
- Poisson ratio for different types of sandstone in different directions can vary from 0.173 to 0.411 (H. Gercek,2006). An average of several typical kinds of sandstone with  $\nu = 0.195$  was used in the thesis. The Poisson ratio of 0.3 for steel is used in the analysis of Dilitant Fault.
- The density of the sandstone is presumed to be 2710 kg/m<sup>3</sup> and the counterpart for steel was taken as 8050 kg/m<sup>3</sup>
- A point load of 750N is applied to the weak section of the Metate Arch along with its self-weight. The value of the load is representing a person with a body

weight of approximately 76.5 kg. The same load is applied to the tip at the top of the Dilitant Fault.

Table 3: Table of Natural Frequencies of First ten Modes in Respect to Approximate Element Size – Metate Arch

$[Element\ Size]^{-1}$	Mode Number									
	1	2	3	4	5	6	7	8	9	10
1551	17.45	20.02	46.82	53.02	61.16	67.54	88.45	92.76	102.56	114.45
2400	15.78	18.10	41.33	48.60	57.65	63.70	77.11	84.05	94.14	106.29
4204	14.61	16.81	38.84	46.37	56.54	62.24	74.14	79.12	87.61	102.80
49891	9.65	12.49	28.52	30.30	43.78	46.68	48.84	52.66	62.44	71.05
307048	7.14	11.41	21.39	22.27	32.74	34.87	37.18	38.52	51.30	55.34
537919	6.40	10.70	19.04	20.59	30.16	32.01	33.26	34.26	44.33	49.87

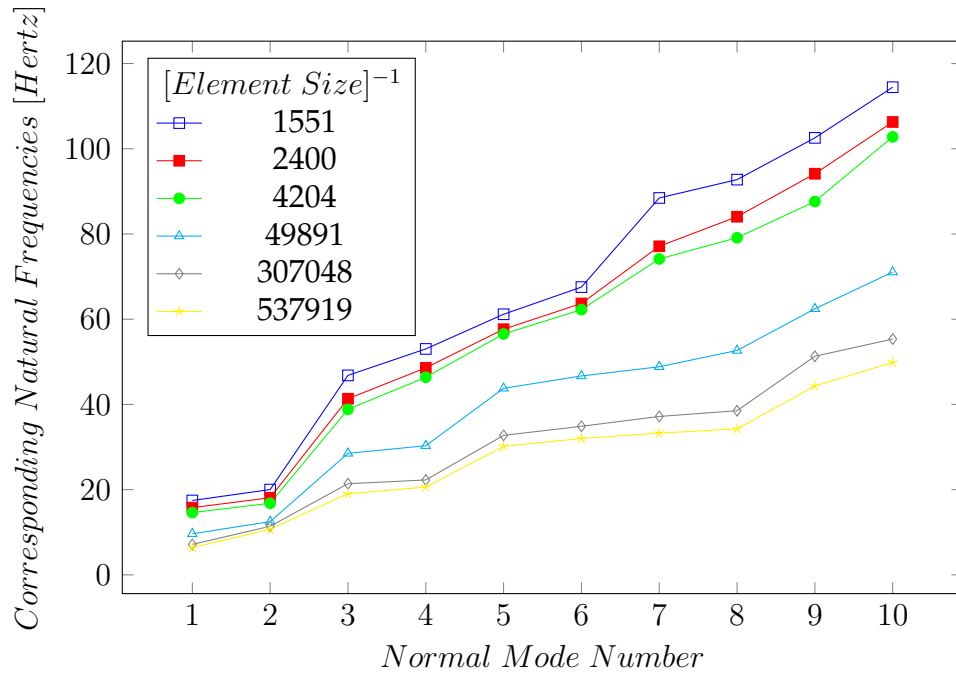
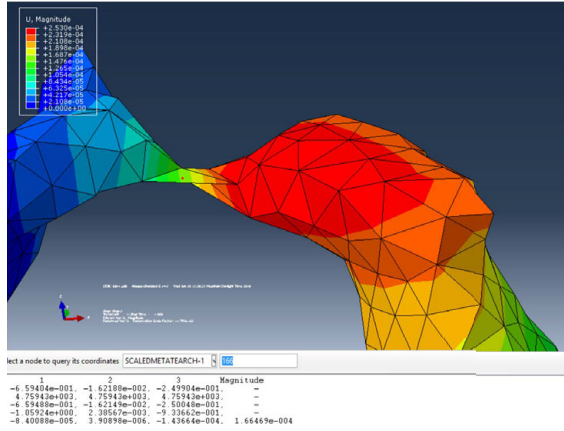
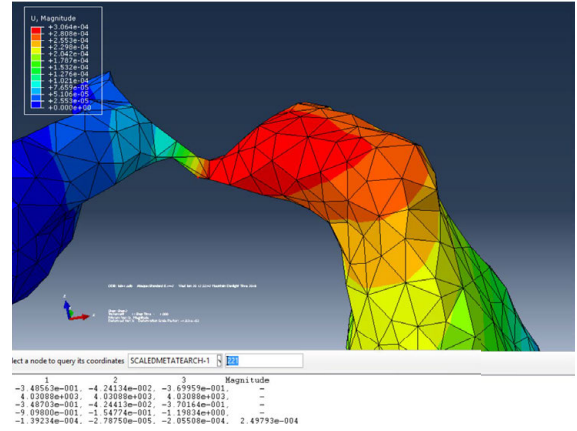


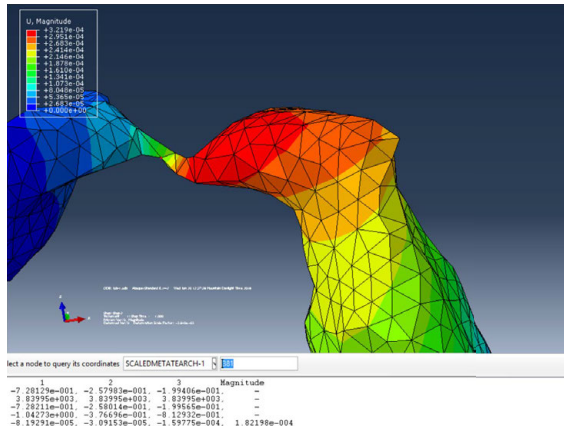
Figure 24: Plot of Natural Frequencies of First ten Modes in Respect to Approximate Element Size – Metate Arch



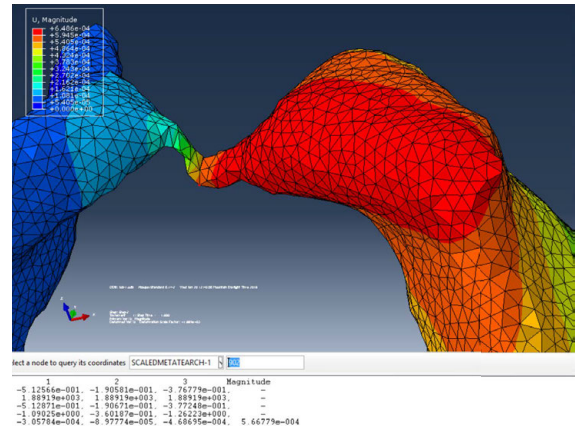
(a)



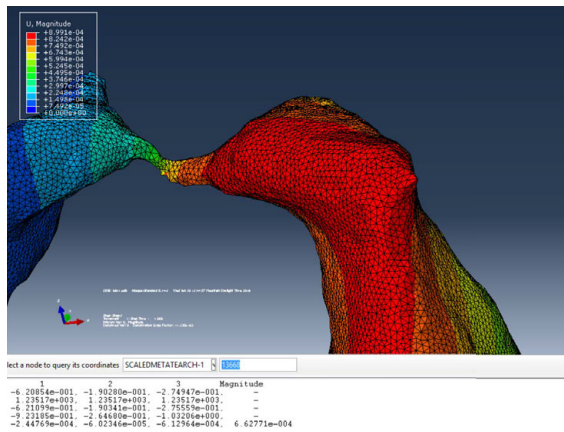
(b)



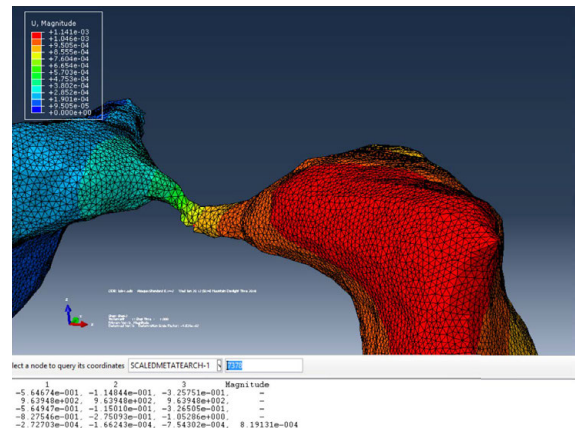
(c)



(d)



(e)



(f)

Figure 25: Stress and Displacement at the Geometric Centroid of the Section with the Smallest Area with Different FE Meshes - Metate Arch

The results of natural frequencies of first ten normal modes of Metate Arch with different FE meshes are listed in Table 3 and plotted in Figure 24. It shows that there is

less discrepancy between the first two computed natural frequencies among the analyses with different meshes compared to the following natural frequencies. As the approximate element size decreases, the convergence of natural frequencies can be found for higher modes.

The result of stress and deformation at the midpoint of Metate Arch under the applied load for different scales of discretization are listed in Table 4. The change of stresses at the mid arch with different sizes of elements can also be seen visually in Figure 25 and the figure (a) through (f) represent models discretized in 7726, 18276, 24860, 36756, 49352, and 58458 elements, respectively. As the approximate sizes of elements decreases, the convergence of stress and deformation can be seen in Figure 26. The red lines are the approximated value for stress and deformation.

Table 4: Stress and Displacement at the Geometric Centroid of the Section with the Smallest Area with Different FE Meshes - Metate Arch

$[Element\ Size]^{-1}$	Displacement (m)	Stress (Pa)
1551	$1.665 \times 10^{-4}$	$9.615 \times 10^5$
2400	$2.498 \times 10^{-4}$	$1.254 \times 10^6$
4204	$1.822 \times 10^{-4}$	$1.348 \times 10^6$
49891	$5.668 \times 10^{-4}$	$3.596 \times 10^6$
307048	$6.628 \times 10^{-4}$	$4.107 \times 10^6$
537919	$8.191 \times 10^{-4}$	$6.754 \times 10^6$

The natural frequencies of first ten normal modes of Dilitant Fault are listed in Table 6 and plotted in Figure 27. Although the natural frequencies of first ten normal modes of Dilitant Fault agree much better than Metate Arch between difference meshes, the graph still follows the same pattern as that of Metate Arch. The difference between the first two natural frequencies between different meshes is negligible while the results from higher modes show larger differences.

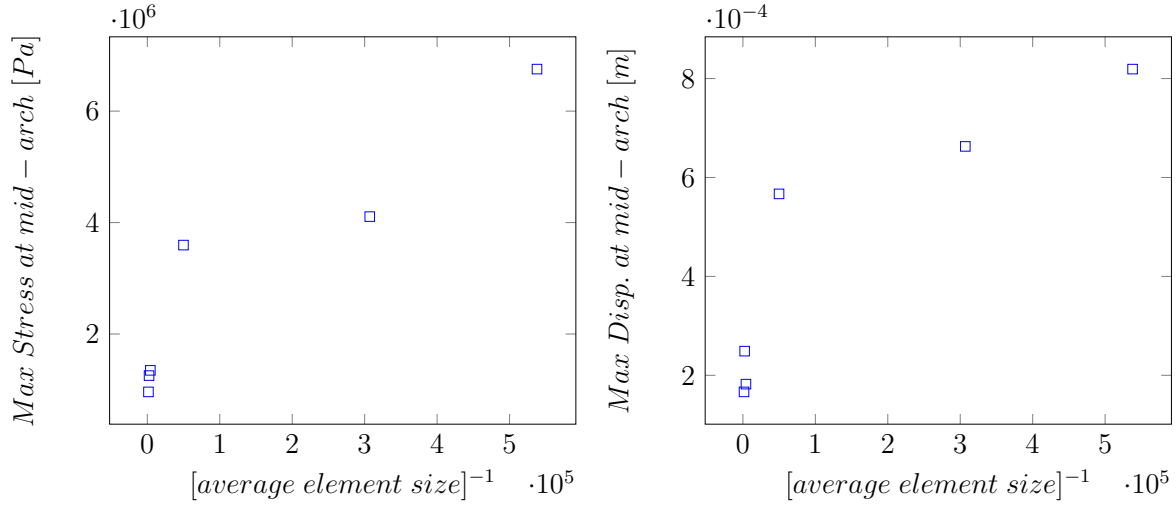


Figure 26: Plot of Stress and Displacement at the Geometric Centroid of the Section with the Smallest Area in Respect to the Inverse of Approximate Element Size – Metate Arch

Figures showing the regions with highest stresses and largest displacements in Dilitant Fault can be found in Appendix A. These data are compiled in Table 6. As the approximate sizes of elements decreases, the convergence of stress and deformation can be seen in Figure 28.

Table 5: Table of Natural Frequencies of First ten Modes in Respect to Approximate Element Size – Dilitant Fault

$[Element\ Size]^{-1}$	Mode Number									
	1	2	3	4	5	6	7	8	9	10
7726	9.96	12.72	17.97	22.34	35.39	40.99	54.04	56.81	88.98	93.61
18276	9.65	12.91	17.26	20.83	34.57	40.60	52.73	54.36	84.90	89.21
24860	9.65	12.91	17.26	20.83	34.57	40.60	52.73	54.36	84.90	88.65
36756	9.67	12.78	16.94	20.54	34.08	40.26	51.88	54.26	83.88	88.02
49352	9.67	12.79	16.65	20.75	33.68	40.27	50.98	54.59	83.60	86.54
58458	9.69	12.83	16.68	20.59	33.70	40.28	50.87	54.14	83.12	86.28

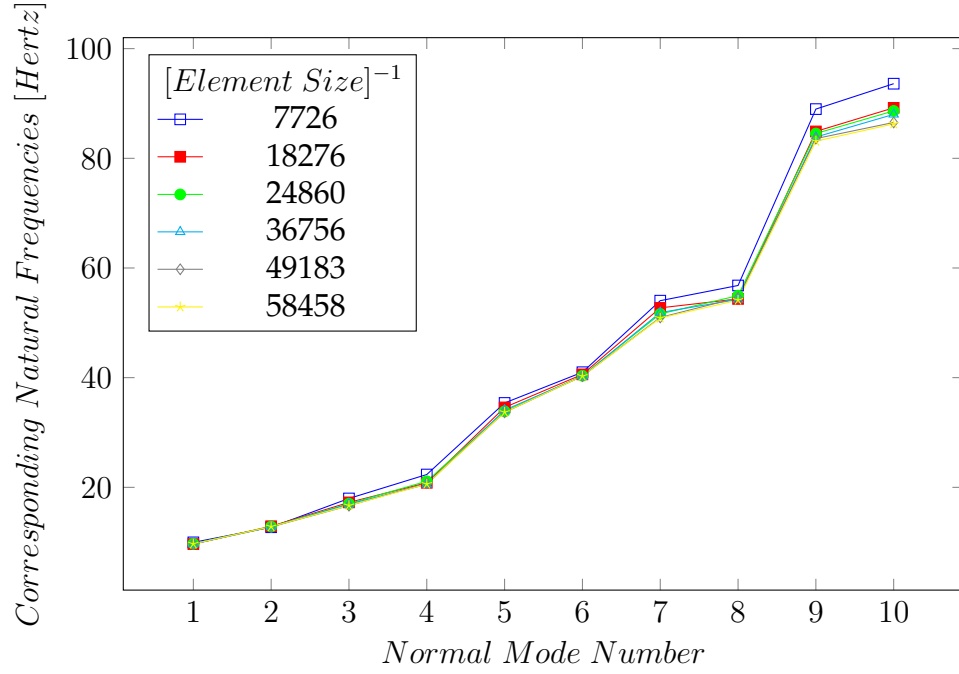


Figure 27: Plot of Natural Frequencies of First ten Modes in Respect to Approximate Element Size – Dilitant Fault

Table 6: Maximum Stress and Displacement Everywhere in Dilitant Fault with Different FE Meshes

$[Element\ Size]^{-1}$	Displacement (m)	Stress (Pa)
7726	$1.997 \times 10^{-3}$	$1.784 \times 10^7$
18276	$1.858 \times 10^{-3}$	$2.32 \times 10^7$
24860	$1.862 \times 10^{-3}$	$2.598 \times 10^7$
36756	$1.906 \times 10^{-3}$	$2.458 \times 10^7$
49183	$1.887 \times 10^{-3}$	$2.696 \times 10^7$
58458	$1.861 \times 10^{-3}$	$2.642 \times 10^7$

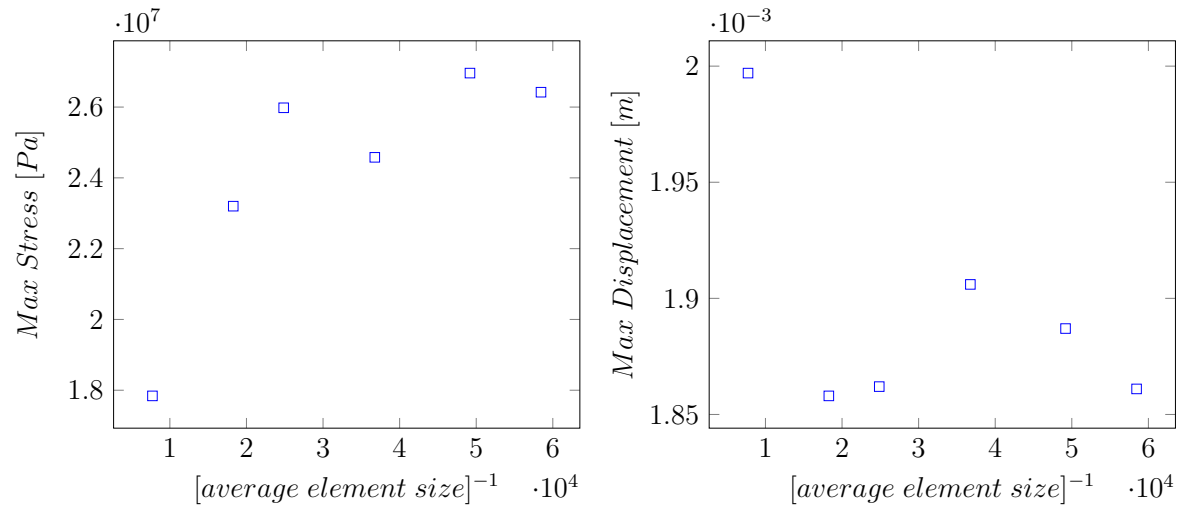


Figure 28: Plot of Stress and Displacement Anywhere in the Model in Respect to the Inverse of Approximate Element Size – Dilitant Fault

Convergence of results of natural frequencies and stress and deformations under applied loads can be seen in both sets of analyses for Metate Arch and Dilitant Fault as the decrease of element size when using 3D model constructed by 2D images. The result supports that the method investigated in this thesis can be feasible for analyses of systems with irregular geometries.



## 4 SUMMARY & CONCLUSION

Models of example systems were constructed to consolidate the application of photogrammetry in 3D modeling for three-dimensional structural mechanics FEM analysis. General steps, and rationales during the modeling process have been fully explained. Systems with unsuccessful results were also discussed to show the requirements and limitations of the method.

The following conditions are recommended for application of the modeling technique investigated to improve the accuracy of the analysis:

- Non-reflective surface of the structure
- Homogeneous material
- Minimum of hollow sections
- Mild and ambient lighting at the scene

Aids from 3D modeling programs can be used to repair the raw 3D models with deficits. If 3D models have any holes and self-intersections, the model will not be able to transform into the compatible model in FEA software packages.

Key steps in the editing of the imported 3D model in Abaqus CAE were introduced to ease the application of this method and eliminate common issue regarding 3D models in Abaqus CAE. Appropriate mesh types need to be chosen to properly discretize the 3D solid model with irregular geometries.

Although the application of the method is some sort of restricted by lighting, the surface of the object, site conditions, etc., proper techniques can be used to help, such as the use of targets and image masks, post-process of photos, improvement of 3D models, etc.

Application of photogrammetry can benefit the quality and productivity of 3D modeling for finite element analysis of structures with complicated geometries. As the number of structures required to be analyzed increases, the saving in time and budget can be substantial. The requirement of intricate 3D model editor programs and related

technique is minimum to achieve the 3D model of structures with complicated geometries.

The quality of the model construction can be improved in different stages along the process, but they were not explicitly investigated. Facilities can be set up at the scene to control the lighting condition when taking the photo sequence. Post-processing of the photos using image editor programs can also adjust the brightness and white balance of the photos without proper lighting. If the target structure is hard to be recognized by the program during alignment process, detailed manual editing of the sparse point cloud can improve the quality of the photo alignment. Elaborating on the quality of alignment may reduce the possibility of having gaps and self-intersection in the constructed models. 3D modeling programs like ZBrush can also be used to directly working on modifying the 3D solid model to enhance its quality before being imported to FEM software packages. Better configuration of the PC allows the program to provide a higher quality of the sparse and dense point cloud. It can provide users with more access to detailed edit of the sparse point cloud and better quality of the dense point cloud thus to directly affect the quality of the 3D surface model.

The application of photogrammetry for 3D modeling in FEM is very promising but there are still barriers to overcome for structures with complex internal layout or various material properties. If the photo sequence can also be taken internally in the structure, a combination of interior and exterior modeling of the structure may be acquired in the future. In addition, the photogrammetric model construction may assist the traditional method to model the external geometry of the structure to minimize manual construction. The advance of photogrammetry and programmatic algorithm in photogrammetric software in the future may also enhance its application in FEM. The development of software and computational ability of PC would also benefit the accuracy and efficiency in reconstructing 3D models of complicated structures. All the procedures of photo alignment, 3D surface model construction, repair of models, and finite element analysis may be integrated into a single program in the future to make the analysis progress fully automatic.

## REFERENCE

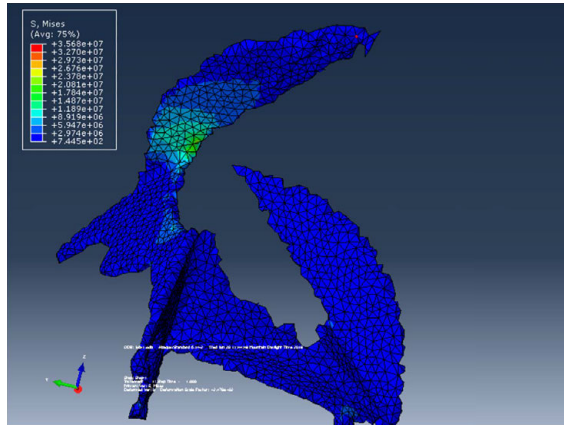
- Agisoft LLC (2011). Agisoft PhotoScan User Manual.
- Ameri, B. and Fritsch, D. (2000). Automatic 3D building reconstruction using plane-roof structures. *ASPRS, Washington DC*.
- Clement, R., Schneider, J., Brambs, H. J., Wunderlich, A., Geiger, M., and Sander, F. G. (2004). Quasi-automatic 3D finite element model generation for individual single-rooted teeth and periodontal ligament. *Computer Methods and Programs in Biomedicine*, 73(2):135–144.
- Conde-Carnero, B., Riveiro, B., Arias, P., and Caamaño, J. C. (2015). Exploitation of Geometric Data provided by Laser Scanning to Create FEM Structural Models of Bridges. *Journal of Performance of Constructed Facilities*, 30(3):4015053.
- Firpo, G., Salvini, R., Francioni, M., and Ranjith, P. G. (2011). Use of Digital Terrestrial Photogrammetry in rocky slope stability analysis by Distinct Elements Numerical Methods. *International Journal of Rock Mechanics and Mining Sciences*, 48(7):1045–1054.
- Hugenholtz, C. H., Whitehead, K., Brown, O. W., Barchyn, T. E., Moorman, B. J., LeClair, A., Riddell, K., and Hamilton, T. (2013). Geomorphological mapping with a small unmanned aircraft system (sUAS): Feature detection and accuracy assessment of a photogrammetrically-derived digital terrain model. *Geomorphology*, 194:16–24.
- Irschara, A., Zach, C., Frahm, J. M., and Bischof, H. (2009). From structure-from-motion point clouds to fast location recognition. *2009 IEEE Computer Society Conference on Computer Vision and Pattern Recognition Workshops, CVPR Workshops 2009*, pages 2599–2606.
- Jiang, R., Jáuregui, D. V., and White, K. R. (2008). Close-range photogrammetry applications in bridge measurement: Literature review. *Measurement: Journal of the International Measurement Confederation*, 41(8):823–834.
- Koutsoudis, A., Vidmar, B., Ioannakis, G., Arnaoutoglou, F., Pavlidis, G., and Chamzas, C. (2014). Multi-image 3D reconstruction data evaluation. *Journal of Cultural Heritage*,

15(1):73–79.

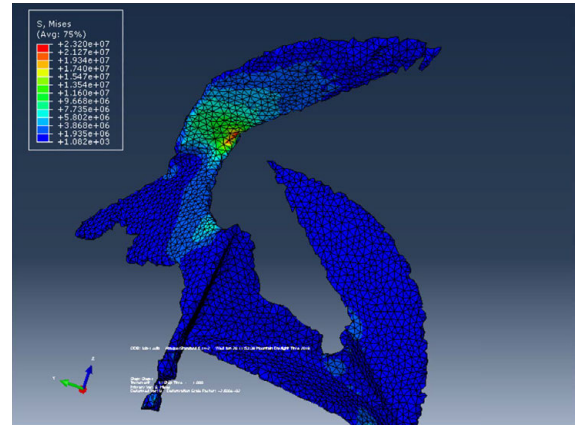
- Lattanzi, D. and Miller, G. R. (2015). 3D Scene Reconstruction for Robotic Bridge Inspection. *Journal of Infrastructure Systems*, 21(2):4014041.
- Lattanzi, D. A. and Miller, G. (2013). A prototype imaging and visualization system for robotic infrastructure inspection. *Structures Congress 2013: Bridging Your Passion with Your Profession*.
- Lubowiecka, I., Armesto, J., Arias, P., and Lorenzo, H. (2009). Historic bridge modelling using laser scanning, ground penetrating radar and finite element methods in the context of structural dynamics. *Engineering Structures*, 31(11):2667–2676.
- Morgan, J. A., Brogan, D. J., and Nelson, P. A. (2017). Application of Structure-from-Motion photogrammetry in laboratory flumes. *Geomorphology*, 276:125–143.
- Park, H. S., Lee, H. M., Adeli, H., and Lee, I. (2007). A new approach for health monitoring of structures: Terrestrial laser scanning. *Computer-Aided Civil and Infrastructure Engineering*, 22(1):19–30.
- Reid, T. R. and Harrison, J. P. (2000). A semi-automated methodology for discontinuity trace detection in digital images of rock mass exposures. *International Journal of Rock Mechanics and Mining Sciences*, 37(7):1073–1089.
- Remondino, F. (2011). Heritage recording and 3D modeling with photogrammetry and 3D scanning. *Remote Sensing*, 3(6):1104–1138.
- Riveiro, B., Caamaño, J. C., Arias, P., and Sanz, E. (2011). Photogrammetric 3D modelling and mechanical analysis of masonry arches: An approach based on a discontinuous model of voussoirs. *Automation in Construction*, 20(4):380–388.
- Ryan, J. C., Hubbard, A. L., Box, J. E., Todd, J., Christoffersen, P., Carr, J. R., Holt, T. O., and Snooke, N. (2015). UAV photogrammetry and structure from motion to assess calving dynamics at Store Glacier, a large outlet draining the Greenland ice sheet. *Cryosphere*, 9(1):1–11.
- Snively, N., Seitz, S., and Szeliski, R. (2006). Photo Tourism: Exploring Photo Collections in 3D. *SIGGRAPH Conference Proceedings*, 1(212):835–846.

- Westoby, M. J., Brasington, J., Glasser, N. F., Hambrey, M. J., and Reynolds, J. M. (2012). 'Structure-from-Motion' photogrammetry: A low-cost, effective tool for geoscience applications. *Geomorphology*, 179:300–314.
- Wu, C. (2013). Towards linear-time incremental structure from motion. *Proceedings - 2013 International Conference on 3D Vision, 3DV 2013*, pages 127–134.
- Wu, C., Agarwal, S., Curless, B., and Seitz, S. M. (2011). Multicore bundle adjustment (mcba). *IEEE Conference on Computer Vision and Pattern Recognition (CVPR)*, (1):5–7.

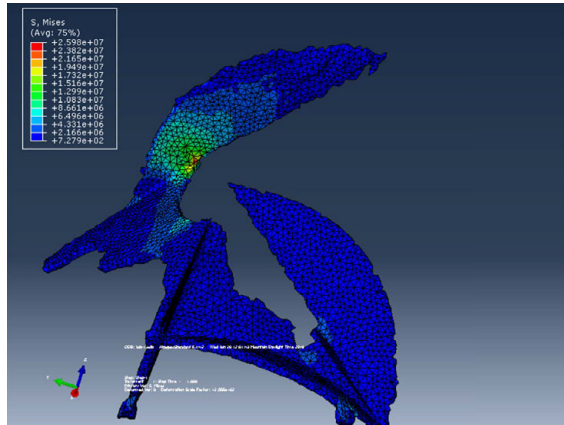
## APPENDIX A: Output Data of Analysis for Dilitant Fault



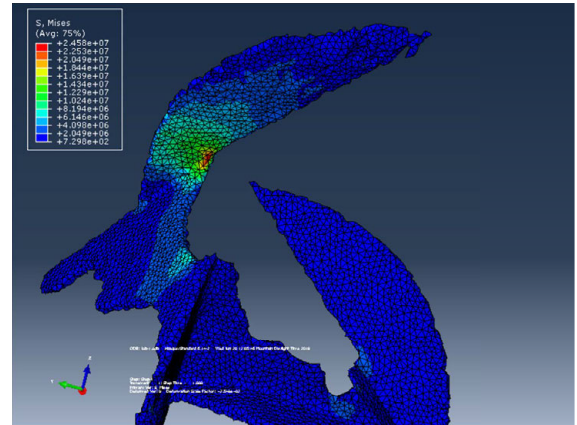
(a)



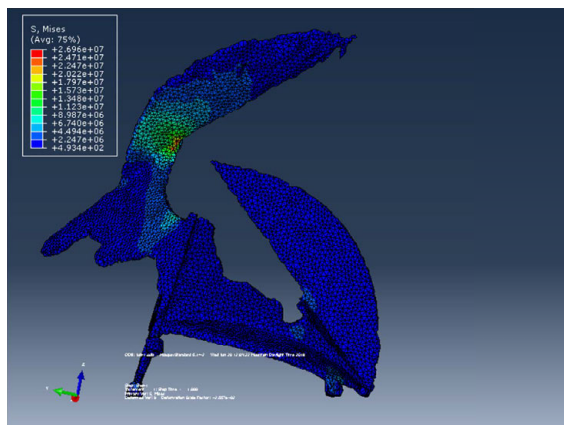
(b)



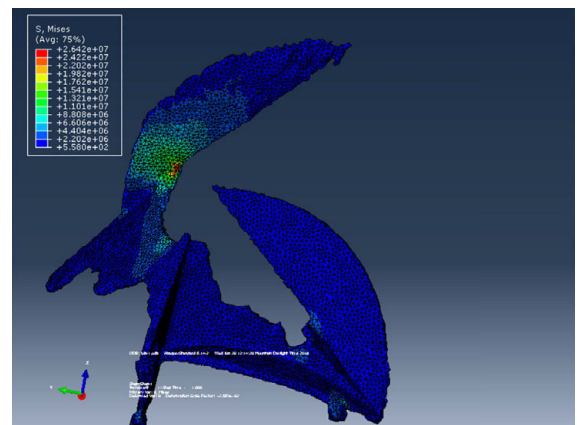
(c)



(d)

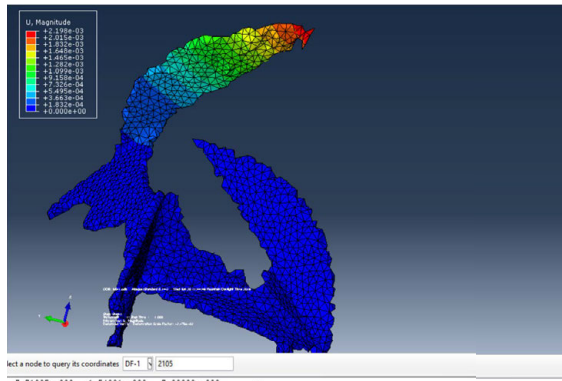


(e)

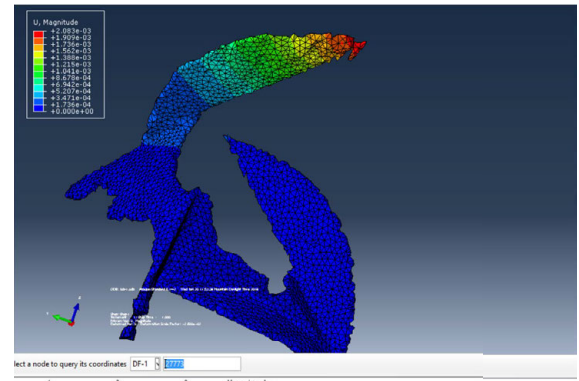


(f)

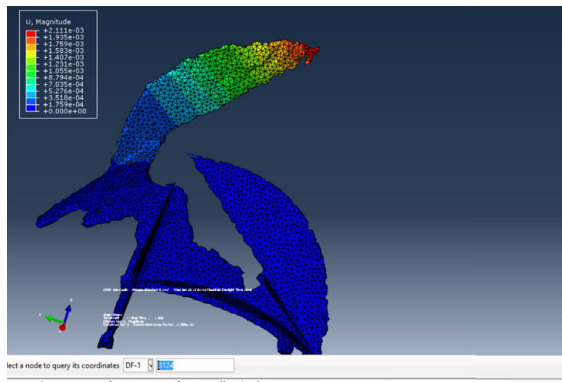
Figure 29: Region with highest stresses in the Dilitant Fault with Meshes of Different Element Sizes



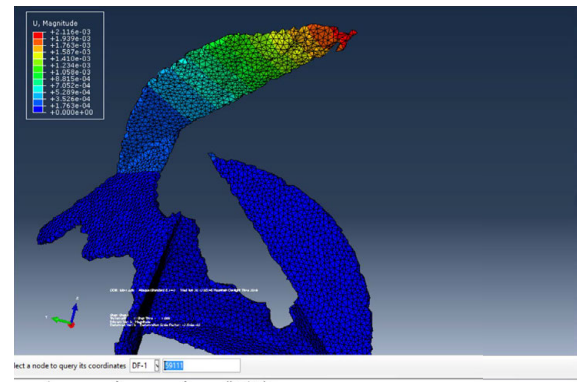
(a)



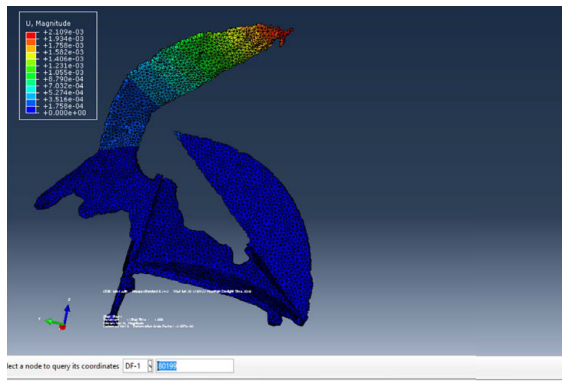
(b)



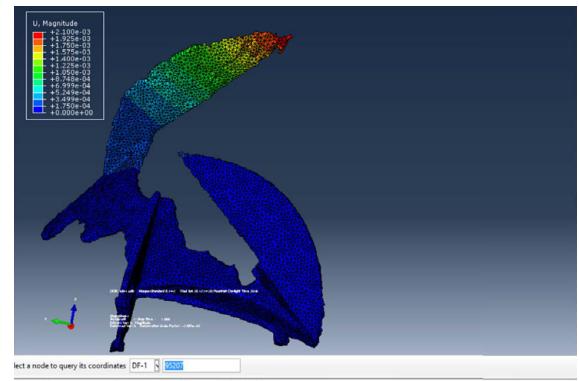
(c)



(d)



(e)



(f)

Figure 30: Region with largest deformation in the Dilatant Fault with Meshes of Different Element Sizes